Assessment of pre-industrial to present-day anthropogenic climate forcing in UKESM1

Fiona M. O'Connor[1], N. Luke Abraham[2,3], Mohit Dalvi[1], Gerd Folberth[1], Paul Griffiths[2,3], Catherine Hardacre[1], Ben T. Johnson[1], Ron Kahana[1], James Keeble[2,3], Byeonghyeon Kim[4], Olaf Morgenstern[5], Jane P. Mulcahy[1], Mark G. Richardson[6], Eddy Robertson[1], Jeongbyn Seo[4], Sungbo Shim[4], Joao C. Teixeira[1], Steven Turnock[1], Jonny Williams[5], Andy Wiltshire[1], and Guang Zeng[5]

[1]Met Office, Exeter, United Kingdom
[2]National Centre for Atmospheric Science, University of Cambridge, United Kingdom
[3]Department of Chemistry, University of Cambridge, United Kingdom
[4]National Institute of Meteorological Sciences, Seogwipo-si, Jeju-do, Korea
[5]National Institute, for Water and Atmospheric Research, Wellington, New Zealand
[6]Centre for Environmental Modelling And Computation, University of Leeds, United Kingdom

Correspondence to: Fiona M. O'Connor (fiona.oconnor@metoffice.gov.uk)

Abstract. Quantifying forcings from anthropogenic perturbations to the Earth System (ES) is important for understanding changes in climate since the pre-industrial period. In this paper, we quantify and analyse a wide range of present-day (PD) anthropogenic climate forcings with the UK's Earth System Model (ESM), UKESM1, following the protocols defined by the Radiative Forcing Model Intercomparison Project (RFMIP) and the Aerosol and Chemistry Model Intercomparison Project (AerChemMIP). In particular, by quantifying effective radiative forcings (ERFs) that include rapid adjustments within a full ESM, it enables the role of various climate-chemistry-aerosol-cloud feedbacks to be quantified.

Global mean ERFs are 1.83, 0.13, -0.33, and 0.93 W m^{-2} at the PD (Year 2014) relative to the pre-industrial (PI; Year 1850) for carbon dioxide, nitrous oxide, ozone-depleting substances, and methane, respectively. The PD total greenhouse gas ERF is 2.89 W m^{-2}, larger than the sum of the individual GHG ERFs.

UKESM1 has an aerosol forcing of -1.13 W m^{-2}. A relatively strong negative forcing from aerosol-cloud interactions and a small negative instantaneous forcing from aerosol-radiation interactions are partially offset by a substantial forcing from black carbon absorption. Internal mixing and chemical interactions mean that neither the forcing from aerosol-radiation interactions nor aerosol-cloud interactions are linear, making the total aerosol ERF less than the sum of the individual speciated aerosol ERFs.

Tropospheric ozone precursors, in addition to exerting a positive forcing due to ozone, lead to oxidant changes which in turn cause an indirect aerosol ERF, altering the sign of the net ERF from nitrogen oxide emissions. Together, aerosol and

tropospheric ozone precursors (near-term climate forcers, NTCFs) exert a global mean ERF of -1.12 W m^{-2}, mainly due to changes in the cloud radiative effect. There is also a negative PD ERF from land use (-0.32 W m^{-2}). It is outside the range of

35   previous estimates, and is most likely due to too strong an albedo response. In combination, the net anthropogenic ERF is potentially biased low (1.61 W m^{-2}) relative to other estimates, due to the inclusion of non-linear feedbacks and ES interactions.

By including feedbacks between greenhouse gases, stratospheric and tropospheric ozone, aerosols, and clouds, some of which act non-linearly, this work demonstrates the importance of ES interactions when quantifying climate forcing. It also suggests

40   that rapid adjustments need to include chemical as well as physical adjustments to fully account for complex ES interactions.

1 Introduction

In order to have a quantitative understanding of past and future climate change, and attribute it and its impacts to different anthropogenic and natural drivers, it is necessary to have a detailed process-based understanding of all aspects of the pathway from anthropogenic (or natural) activity through to climate response and impacts. A key mechanism for addressing this

45   overarching objective is the 6th Coupled Model Intercomparison Project (CMIP6; Eyring et al., 2016), which designs and distributes data from multi-model simulations. These simulations, with state-of-the-art climate models or Earth System Models (ESMs), are aimed at addressing these important climate science questions directly or via dedicated CMIP6-endorsed model intercomparison projects (MIPs) such as the Aerosol and Chemistry Model Intercomparison Project (AerChemMIP; Collins et al., 2017). The first part of this cause-effect chain from activity to climate response, mediated through the atmosphere and

50   the land surface, is quantifying changes to the Earth's radiation budget, often termed radiative forcing.

Successive assessment reports of the Intergovernmental Panel on Climate Change (IPCC) have used the concept of radiative forcing (RF) as a metric to quantify the effects of different anthropogenic and natural drivers on the Earth's radiation balance. For this purpose, radiative forcing (RF), or more precisely, the stratospherically-adjusted radiative forcing (SARF) is defined

55   at the tropopause (Myhre et al., 2013a) as:

$$RF = IRF + A_{strattemp} \qquad , \qquad\qquad (1)$$

where IRF is the instantaneous radiative forcing and $A_{strattemp}$ is the additional change in the net downward radiative fluxes at

60   the tropopause solely due to stratospheric temperature adjustment (Hansen et al., 1997), while holding all other variables fixed. Including the stratospheric temperature adjustment can significantly affect the magnitude of a forcing (e.g. Smith et al., 2018) and even change the sign of the forcing in the case of ozone depletion (Shine et al., 1995). As a result, RF rather than IRF is a better predictor of the drivers of global mean temperature. RF is part of a framework, based around energy budget analyses, that has split forcing from climate response (Boucher et al., 2013; Myhre et al., 2013a; Sherwood et al., 2015). It's been used

65   extensively to evaluate and compare the strength of the various mechanisms, both anthropogenic and natural, affecting the
      Earth's radiation balance and hence, their contribution to climate change (e.g. Hansen et al., 1997; Shine and Forster, 1999).
      However, despite the extensive use of RF as a metric for climate change, it is often calculated inconsistently between the
      different drivers of climate change (e.g. Myhre et al., 2013a) and participating models in the 5th Coupled Model
      Intercomparison Project (CMIP5; Taylor et al., 2012) can show large differences in forcing (Andrews et al., 2012a; Forster et
70   al., 2013). For example, the RF attributed to long-lived greenhouse gases (LLGHGs) is typically based on changes in observed
      concentrations between the pre-industrial (PI) and the present day (PD) and using line-by-line radiative transfer calculations
      and/or simple, yet justified, expressions for RF based on Myhre et al. (1998) and Ramaswamy et al. (2001). These expressions
      have been updated for some LLGHGs recently (Etminan et al., 2016). However, the observed concentrations themselves may
      be subject to biogeochemical feedbacks (e.g. Arneth et al., 2010; O'Connor et al., 2010) and observational-based estimates of
75   forcing are also relatively uncertain (Skeie et al., 2011).

      In contrast to the quantification of the LLGHG RF, the RF from tropospheric ozone (O_3) changes at the PD relative to the PI
      (Stevenson et al., 2013) is based solely on models. It has been calculated using the ensemble of models (Young et al., 2013)
      participating in the Atmospheric Chemistry and Climate Model Intercomparison Project (ACCMIP; Lamarque et al., 2013)
80   providing input to offline radiative transfer models (e.g. Edwards and Slingo, 1996). The simulations used the corresponding
      sea surface temperatures (SSTs) and sea ice (SI) conditions for the time periods of interest (PI and PD), including some climate
      response and feedbacks at the PD, meaning that the resulting RF doesn't fit into the simple forcing-feedback framework,
      whereby feedbacks are related to global mean temperature change and forcings are not (Sherwood et al., 2015). There are also
      additional uncertainties associated with the estimate of tropospheric O_3 RF due to the lack of a robust and reliable observational
85   constraint for PI O_3 concentrations (e.g. Stevenson et al., 2013), the diversity in modelled PD tropospheric O_3 burden across
      multi-model ensembles (e.g. Young et al., 2013; Young et al., 2018), uncertainties in historical emissions of tropospheric O_3
      precursors, and the apparent inability of current state-of-the-art chemistry models to replicate near-recent observed trends in
      tropospheric O_3 (Parrish et al., 2014; Young et al., 2018) although recently, isotopic measurements seem to corroborate the
      modelled trends (Yeung et al., 2019). Additional uncertainties in Stevenson et al. (2013) arise from neglecting the change in
90   O_3 in the lower stratosphere attributable to changes in tropospheric O_3 precursors and the contribution from stratospheric O_3
      depletion on the modelled changes in tropospheric O_3. Despite these uncertainties in tropospheric O_3 RF, the even larger
      uncertainty in aerosol forcing (Myhre et al., 2013a; Bellouin et al., 2019) accounts for the majority of the uncertainty in the
      total anthropogenic forcing.
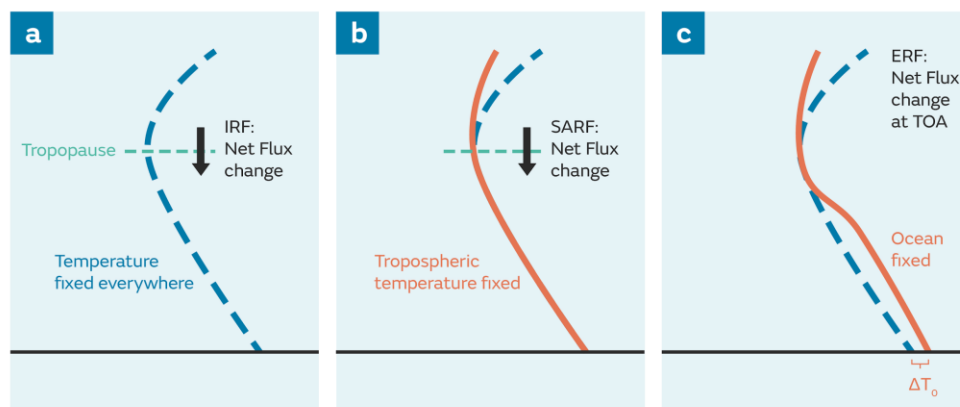
95

Figure 1: Schematic showing the different definitions of radiative forcing: a) instantaneous radiative forcing (IRF), b) stratospherically-adjusted radiative forcing (SARF), and c) effective radiative forcing (ERF). IRF and SARF are typically defined at the tropopause whereas ERF is defined at the top of atmosphere (TOA). Adapted from Fig. 8.1 of the IPCC 5th assessment report (Myhre et al., 2013a), which in turn was updated from Hansen et al. (2005).

100

Although RF has been calculated inconsistently between the different drivers of climate change to date, the fifth assessment report (AR5) of the IPCC also adopted an extension to the definition of radiative forcing to include fast feedbacks or rapid adjustments other than the stratospheric temperature adjustment. This updated definition, the effective radiative forcing (ERF), is now the preferred metric of choice for ranking the drivers of climate change. ERF is defined at the top of the atmosphere

105 (TOA), following Chung and Soden (2015), as:

$$ERF = IRF + \sum_i A_i \qquad , \qquad\qquad (2)$$

where IRF is the instantaneous radiative forcing at the TOA following a perturbation and A_i is a rapid adjustment in the

110 atmosphere or over the land that alters the net downward radiative flux at the TOA either positively or negatively. These adjustments include changes in stratospheric temperatures (as included in the definition of RF or SARF above; Eqn. 1) as well as adjustments such as tropospheric temperatures, water vapour, clouds, and land surface albedo, as examples, but global mean surface temperatures or global ocean conditions remain unchanged. Although the error associated with an ERF tends to be larger than that of RF (or SARF), climate sensitivity parameters (i.e. the degree of warming per unit forcing) are less dependent

115 on the forcing agent and it is more representative of the climate response than the traditional RF (Forster et al., 2016). For example, rapid adjustments lead to the ERF for black carbon (BC) being half that of its IRF (Stjern et al., 2017; Smith et al., 2018). On the other hand, Xia et al. (2016) found that cloud and sea ice feedbacks driven by stratospheric O_3 recovery included in the ERF definition lead to a significant adjustment that changes the sign and magnitude of the stratospheric O_3 forcing from the SARF. Although the definitions of RF and ERF differ in where the change in radiative fluxes is diagnosed, ERFs at the

120 tropopause are nearly identical to those at the TOA for tropospheric forcing agents; this is also the case for SARFs. An overview

of the historical evolution of the RF concept, its quantification for different forcing agents, and applications of RF can be found in Ramaswamy et al. (2019).

The use of ERF as a metric also offers the advantage that it can be readily calculated using a pair of parallel simulations with
125   standard model TOA radiative flux diagnostics (Forster et al., 2016) albeit with a requirement to run for relatively long periods (~30 years) to reduce the uncertainty associated with meteorological variability (e.g. Shindell et al., 2013a). Despite this requirement, it has now become the metric of choice over RF (Boucher et al., 2013) to rank the drivers of climate change. Figure 1 illustrates the various definitions of radiative forcing, including those of IRF, SARF (or RF), and ERF.

130   The aim of the current study is to quantify the PI (Year 1850) to PD (Year 2014) effective radiative forcings (ERFs) from anthropogenic drivers of climate change with a fully coupled Earth System Model (ESM). Using the experimental protocol recommended for the Radiative Forcing Model Intercomparison Project (RFMIP; Pincus et al., 2016), PD forcings will be quantified relative to the PI from changes in emissions, concentrations, and/or land use due to anthropogenic activities. This approach offers a consistent methodology for diagnosing the ERFs of all forcing agents or Earth System (ES) perturbations
135   and, if applied consistently across all models as part of the 6th Coupled Model Intercomparison Project (CMIP6; Eyring et al., 2016), should help to address some of the deficiencies and uncertainties associated with previous estimates of forcing (e.g. Myhre et al., 2013a) and improve our understanding of how the ES responds to forcing (Pincus et al., 2016). The paper is organised as follows. Section 2 provides a brief description of the UK's Earth System Model, UKESM1, used in this study. Section 3 outlines the experimental setup and the simulations carried out. PD anthropogenic forcings relative to PI are presented
140   in Sect. 4, while conclusions can be found in Sect. 5.

2 Model Description

The model used in this study is the atmospheric and land components of the UK's Earth System Model, UKESM1 (Sellar et al., 2019). UKESM1 is based on the Global Atmosphere 7.1/Global Land 7.0 (GA7.1/GL7.0; Walters et al., 2019) configuration of the Hadley Centre Global Environment Model version 3 (HadGEM3; Hewitt et al., 2011), herein referred to
145   as HadGEM3-GA7.1, to which terrestrial carbon/nitrogen cycles (Sellar et al., 2019) and interactive stratosphere-troposphere chemistry (Archibald et al., 2019) from the UK Chemistry and Aerosol (UKCA; Morgenstern et al., 2009; O'Connor et al., 2014) model have been coupled. The model resolution is N96L85; this is equivalent to a horizontal resolution of roughly 135 km and the 85 terrain-following model levels cover an altitude range up to 85 km above sea level. The physical atmosphere model, HadGEM3-GA7.1, already includes the UKCA prognostic aerosol scheme called GLOMAP-mode (Mann et al., 2010;
150   Mulcahy et al., 2018), in which secondary aerosol formation is determined by prescribed oxidant fields. Here, the UKCA chemistry and aerosol schemes are coupled, with oxidants from the stratosphere-troposphere chemistry scheme (Archibald et al., 2019) determining secondary aerosol formation rates. A full description and evaluation of the UKCA chemistry and aerosol

schemes in UKESM1 can be found in Archibald et al. (2019) and Mulcahy et al. (2019), respectively. Mulcahy et al. (2018) also implemented a number of aerosol process improvements in HadGEM3-GA7.1 which helped to address the strong negative

155   PD aerosol forcings from its predecessor model (i.e. HadGEM3-GA7.0; Walters et al., 2019).

3 Model Setup and Experiments

To calculate the pre-industrial (PI; Year 1850) to present-day (PD; Year 2014) effective radiative forcings (ERFs) due to a PI-to-PD perturbation (e.g. change in emissions), timeslice experiments with fixed sea surface temperatures (SSTs) and sea ice (SI) were carried out, following the protocol defined by the Radiative Forcing Model Intercomparison Project (RFMIP; Pincus

160   et al., 2016). The experimental setup was also consistent with recommendations from Forster et al. (2016) and the protocol for timeslice ERF experiments defined in the Aerosol and Chemistry Model Intercomparison Project (AerChemMIP; Collins et al., 2017).

Experiment ID	MIP	CO₂	N₂O	HCs	CH₄	Aerosol precursors	Trop. O₃ precursors	Land use
piClim-control	AerChemMIP; RFMIP	1850	1850	1850	1850	1850	1850	1850
piClim-CO2	N/A	2014	1850	1850	1850	1850	1850	1850
piClim-CO2phys[a]	N/A	2014 (land surface) 1850 (radiation)	1850	1850	1850	1850	1850	1850
piClim-4xCO2	RFMIP	4x1850	1850	1850	1850	1850	1850	1850
piClim-N2O	AerChemMIP	1850	2014	1850	1850	1850	1850	1850
piClim-HC	AerChemMIP	1850	1850	2014	1850	1850	1850	1850
piClim-CH4	AerChemMIP	1850	1850	1850	2014	1850	1850	1850
piClim-GHG	RFMIP	2014	2014	2014	2014	1850	1850	1850
piClim-SO2	AerChemMIP	1850	1850	1850	1850	2014 (SO2); 1850 (non-SO2)	1850	1850
piClim-BC	AerChemMIP	1850	1850	1850	1850	2014 (BC); 1850 (non-BC)	1850	1850

piClim-OC	AerChemMIP	1850	1850	1850	1850	2014 (OC); 1850 (non-OC)	1850	1850
piClim-aer	AerChemMIP	1850	1850	1850	1850	2014	1850	1850
piClim-NOx	AerChemMIP	1850	1850	1850	1850	1850	2014 (NOx); 1850 (non-NOx)	1850
piClim-VOC	AerChemMIP	1850	1850	1850	1850	1850	2014 (VOC); 1850 (non-VOC)	1850
piClim-O3	AerChemMIP	1850	1850	1850	1850	1850	2014	1850
piClim-NTCF[b]	AerChemMIP	1850	1850	1850	1850	2014	2014	1850
piClim-LU	RFMIP	1850	1850	1850	1850	1850	1850	2014
piClim-Anthro	RFMIP	2014	2014	2014	2014	2014	2014	2014

165

Table 1: List of all the fixed sea surface temperature (fSST) effective radiative forcing (ERF) experiments carried out with the UK's Earth System Model, UKESM1, to diagnose the pre-industrial to present-day ERFs from changes in emissions, concentrations and/or land use. Each simulation was 45 years in length, with analysis based on the last 30 years. [a]In the *piClim-CO2phys* simulation, only the land surface sees the PI-to-PD perturbation in CO_2, the radiation scheme still sees the PI concentration. [b]The AerChemMIP experiment *piClim-NTCF* is also known as *piClim-aerO3* in RFMIP.

170

Effectively, this involves running a PI timeslice experiment, called *piClim-control* here, in which SSTs and SI and all forcings were fixed at year-1850 levels. The SSTs and SI used in *piClim-control* were monthly time-varying climatologies derived from 30 years (i.e. Years 2156-2185 inclusive) of output from the UKESM1 pre-industrial coupled control experiment (*piControl*)

175 characterised in Sellar et al. (2019) and one of an underpinning set of coupled experiments for CMIP6 (Eyring et al., 2016). It also used 30-year monthly mean climatologies for the vegetation distribution, canopy height, leaf area index, surface seawater dimethyl sulphide (DMS) and chlorophyll concentrations derived from the same period of *piControl*. Fixing the vegetation distribution was not included in the RFMIP protocol and any potential vegetation rapid adjustments will be somewhat constrained. This is due to the simulations being based on the configuration of UKESM1 used for the Atmosphere Model

180 Intercomparison Project (AMIP) simulation (which prescribed vegetation characteristics). Although the AerChemMIP protocol (Collins et al., 2017) requested use of the maximum capability possible, interactive vegetation was not a model requirement. The extra RFMIP experiments carried out here were only done as a late addition and the same experimental setup was kept for internal consistency.

185 The model was initialised using output from the start of the 30-year period used to produce the PI climatologies (i.e. January 2156 of *piControl*). All the other experiments are perturbation experiments, parallel to *piClim-control*, in which selected

emissions, concentrations and/or land use were changed from year-1850 to year-2014 values. Although AerChemMIP and RFMIP recommend 30 years for fixed SST timeslice ERF experiments, the perturbations to the LLGHGs took up to 15 years to propagate fully into the stratosphere due to the turnover timescale associated with the Brewer-Dobson circulation (e.g.
190 Butchart, 2014). Therefore, all simulations were 45 years in length. Using the latter 30 years of the paired simulations, the ERFs from the PI-to-PD perturbations were diagnosed as the time-mean global-mean difference in the TOA net radiative fluxes. Details on how the ERF was further decomposed can be found in Sect. 3.1.

In all cases, the emissions and/or GHG concentrations for 1850 and 2014 were taken from Hoesly et al. (2018), van Marle et
195 al. (2017), and Meinhausen et al. (2017). For prescribing the anthropogenic land use change at 2014, the difference in vegetation between 1850 and 2014 was taken from a UKESM1 coupled historical simulation, in which the only transient forcing was anthropogenic land use change. Natural volcanic and solar forcings were fixed in all simulations at 1850 levels (Arfeuille et al., 2014; Thomason et al., 2018; Matthes et al., 2017) using those specified for CMIP6 (Eyring et al., 2016). Table 1 gives a full list of the fixed SST ERF experiments carried out with UKESM1 for this study. The only experiment
200 omitted from the fixed SST ERF experiments specified in the RFMIP and AerChemMIP protocols is *piClim-NH3*; this is because UKESM1's aerosol scheme, GLOMAP-mode (Mann et al., 2010; Mulcahy et al., 2018; Mulcahy et al., 2019), does not include any treatment for ammonium nitrate.

Through a partnership between the Met Office Hadley Centre (MOHC; https://www.metoffice.gov.uk/climate-
205 guide/science/science-behind-climate-change/hadley), the UK's National Centre for Atmospheric Science (NCAS; https://www.ncas.ac.uk/en/), New Zealand's National Institute for Water and Atmospheric Research (NIWA; https://www.niwa.co.nz/), and National Institute of Meteorological Science/Korean Meteorological Administration (NIMS-KMA; http://nims.go.kr/MA/main.jsp), the fixed SST ERF experiments carried out with UKESM1 were spread across multiple high performance computing (HPC) platforms. Due to the non-linearity of the equations being solved, ESMs are sensitive to
210 the propagation of small perturbations. This makes the simulations sensitive to changes in platform that cannot guarantee bit reproducible results. Considering that the RFMIP/AerChemMIP experiments were spread across 3 different HPC platforms, we aimed to verify that the output from the atmosphere-only configuration of UKESM1 was scientifically consistent with each other.

215 To test this, we created an ensemble of short runs on each machine by perturbing selected variables in their initial conditions, using a perturbation with a numerical value comparable to the machines precision. The spread of results (at each point in time and space) on each platform was then used to determine whether they could each have been sampled from the same ensemble of results generated on either machine. A permutation method was used to ensure statistical independence between neighbouring points according to the work described by Wilks (1997). A paper, describing this protocol in more detail, is in
220 preparation (Teixeira et al., 2019). Further to this, a number of perturbation experiments were carried out in duplicate to test

the sensitivity of the global mean ERFs to differences in HPC platform. These duplicate experiments are listed in Table 2 and will be available through the Earth System Grid Federation (ESGF; https://esgf.llnl.gov/) archive as different realisations of the same experiment.

HPC	Compiler	Experiment ID	Realisation
Met Office CrayXC40	Cray compiling environment 8.3.4	*piClim-control*	1
		piClim-SO2	2
		piClim-OC	2
		piClim-NTCF	2
NIWA XC50	Intel Compilers 17.0.4 20170411	*piClim-SO2*	1
		piClim-OC	1
KMA Cray XC40	Cray compiling environment 8.3.7	*piClim-NTCF*	1

225

Table 2: List of atmosphere-only PI control (*piClim-control*) and duplicate fixed sea surface temperature (fSST) perturbation experiments (*piClim-X*) carried out with the UK's Earth System Model, UKESM1, on different high performance computing (HPC) platforms.

4 Present-Day Anthropogenic Effective Radiative Forcings

230 The ERF has been calculated from the difference (Δ) in the net TOA radiative flux (F) between the perturbed simulation (e.g. *piClim-CH4;* Table 1) and the *piClim-control* simulation as follows:

$$ERF = \Delta F \qquad . \qquad\qquad\qquad (3)$$

This can be decomposed into the clear-sky (CS) ERF ($ERFcs$) and the change in the Cloud-Radiative Effect (ΔCRE) using

235 the diagnosed CS radiative flux ($Fclear$):

$$ERF = \Delta Fclear + \Delta(F - Fclear) \qquad\qquad (4)$$
$$= ERFcs + \Delta CRE \qquad . \qquad\qquad (5)$$

240   However, many of the experiments in this study either perturb aerosol emissions and/or alter aerosol concentrations via chemical and dynamical feedbacks. Changes in aerosol can bias the diagnosed CRE as aerosol scattering and absorption typically reduce the contrast in shortwave (SW) reflection between cloudy and clear-sky scenes; a process termed "cloud masking" (e.g. Zelinka et al., 2014). In consideration of this, we have calculated the change in CRE from "clean" radiation calls that exclude aerosol-radiation interactions (ari), as recommended in Ghan (2013):

245

$$ERF = \Delta(F - Fclean) + \Delta Fclear, clean + \Delta(Fclean - Fclear, clean) \qquad (6)$$
$$= Aerosol\ IRF\ +\ ERFcs, clean\ +\ \Delta CRE' \qquad (7)$$
$$= ERFcs'\ +\ \Delta CRE' \qquad . \qquad (8)$$

250   The ERF is thus separated into a component due to cloud property changes ($\Delta CRE'$) and the non-cloud forcing ($ERFcs'$). Here, $ERFcs'$ is the sum of the aerosol IRF and any non-aerosol changes in CS flux and differs slightly from $ERFcs$ in equation (5), in that it can include the impact of aerosol scattering and absorption in the clear-air above or below clouds. One acknowledged limitation is that variations in gaseous absorption and emission between clear and cloudy scenes also lead to cloud masking effects (e.g. Soden et al., 2008). Although Ghan's method removes the very prominent influence of aerosols,
255   cloud-masking from ozone (O_3) and GHGs may still affect the separation of ERF into the CS and CRE components.

4.1 Overview of Present-Day Effective Radiative Forcings (ERFs)

The effective radiative forcing (ERF), clear-sky (CS), and cloud radiative effect (CRE) contributions, following equations (6) to (8) are listed in Table 3 for all perturbation experiments relative to *piClim-control*, and are further decomposed into the SW (solar), LW (terrestrial) and net (SW + LW) components. The global mean ERFs are also plotted in Fig. 2. Together, they
260   show that the global mean PD ERF by greenhouse gases (GHGs) is +2.89 ± 0.04 W m^{-2}, which is offset by an aerosol ERF of -1.13 ± 0.04 W m^{-2}. These estimates are consistent with ERFs of +3.09 and -1.10 W m^{-2}, respectively (Andrews et al., 2019), from the HadGEM3 GC3.1 (Williams et al., 2017) physical model (herein referred to as HadGEM3-GC3.1) upon which UKESM1 is based and with the range of previous estimates (e.g. Myhre et al., 2013a). The net anthropogenic ERF is +1.61 W m^{-2}, again consistent with the range of estimates from AR5 (Myhre et al., 2013a) but less than the estimate from HadGEM3-
265   GC3.1 (+1.81 W m^{-2}; Andrews et al., 2019) by nearly 0.2 W m^{-2}; this is largely due to the land use ERF in UKESM1 being more strongly negative than in HadGEM3-GC3.1 by 0.21 W m^{-2}. The net anthropogenic ERF quantified here is also narrowly outside the range of total historical radiative forcing of 2.3 (+1.7 to +3.0) [5-95%] W m^{-2} (Andrews and Forster, 2019) derived from energy budget constraints.

PI-to-PD Perturbation	Effective radiative forcings from 1850 to 2014 (W m⁻²)						
	NET ERF	**LWcs'**	**SWcs'**	**LW △CRE'**	**SW △CRE'**	**NETcs'**	**NET △CRE'**
CO2	+1.82 ±0.04	+1.56 ±0.02	+0.12 ±0.02	-0.35 ±0.02	0.50 ±0.03	+1.68 ±0.03	+0.14 ±0.03
CO2phys	+0.008 ±0.04	-0.065 ±0.03	-0.019 ±0.02	-0.021 ±0.02	+0.112 ±0.02	-0.083 ±0.03	+0.09 ±0.02
4xCO2	+7.88 ±0.04	+6.80 ±0.03	+0.49 ±0.02	-1.55 ±0.02	+2.14 ±0.02	+7.29 ±0.02	+0.60 ±0.02
N2O	+0.13 ±0.03	+0.25 ±0.03	-0.03 ±0.02	-0.13 ±0.02	+0.03 ±0.03	+0.22 ±0.03	-0.10 ±0.03
HC	-0.33 ±0.04	+0.37 ±0.02	-0.43 ±0.02	+0.23 ±0.02	-0.50 ±0.03	-0.06 ±0.02	-0.27 ±0.02
CH4	+0.93 ±0.04	+0.73 ±0.02	+0.12 ±0.01	-0.39 ±0.02	+0.48 ±0.03	+0.85 ±0.03	+0.08 ±0.03
GHG	+2.89 ±0.04	+3.08 ±0.02	-0.16 ±0.02	-0.65 ±0.02	+0.62 ±0.03	+2.92 ±0.02	-0.01 ±0.03
SO2	-1.45 ±0.03	+0.14 ±0.03	-0.60 ±0.02	0.18 ±0.01	-1.17 ±0.03	-0.46 ±0.03	-0.99 ±0.02
BC	+0.32 ±0.04	-0.00 ±0.02	+0.38 ±0.02	-0.18 ±0.01	+0.12 ±0.03	+0.38 ±0.03	-0.06 ±0.02
OC	-0.27 ±0.03	-0.01 ±0.02	-0.17 ±0.02	+0.01 ±0.02	-0.09 ±0.03	-0.18 ±0.02	-0.09 ±0.02
Aer	-1.13 ±0.04	+0.17 ±0.02	-0.28 ±0.02	-0.02 ±0.01	-1.00 ±0.03	-0.11 ±0.02	-1.02 ±0.03
NOx	-0.08 ±0.04	+0.02 ±0.03	+0.02 ±0.02	-0.02 ±0.01	-0.11 ±0.02	+0.04 ±0.03	-0.13 ±0.02
VOC	+0.21 ±0.04	+0.08 ±0.03	+0.01 ±0.02	-0.08 ±0.02	+0.20 ±0.03	+0.09 ±0.03	+0.12 ±0.03
O3	+0.15 ±0.04	+0.11 ±0.02	+0.05 ±0.02	-0.10 ±0.02	+0.10 ±0.03	+0.16 ±0.03	-0.01 ±0.03
NTCF	-1.12	+0.24	-0.29	-0.06	-1.02	-0.04	-1.08

	±0.03	±0.02	±0.02	±0.02	±0.03	±0.03	±0.02
LU	-0.32 ±0.04	+0.05 ±0.03	-0.46 ±0.02	+0.01 ±0.01	+0.07 ±0.02	-0.40 ±0.03	+0.09 ±0.02
Anthro	+1.61 ±0.03	+3.38 ±0.02	-0.87 ±0.02	-0.66 ±0.02	-0.24 ±0.02	+2.50 ±0.03	-0.89 ±0.02

270

Table 3: Present-day (PD; Year 2014) effective radiative forcings (ERFs) of climate relative to pre-industrial (PI; Year 1850) in W m^{-2} derived from Equations (6) to (8), and including an estimate of the standard error (Forster et al., 2016). Where duplicate experiments exist (e.g. *piClim-SO2***), the quoted ERFs use Realisations 2.**
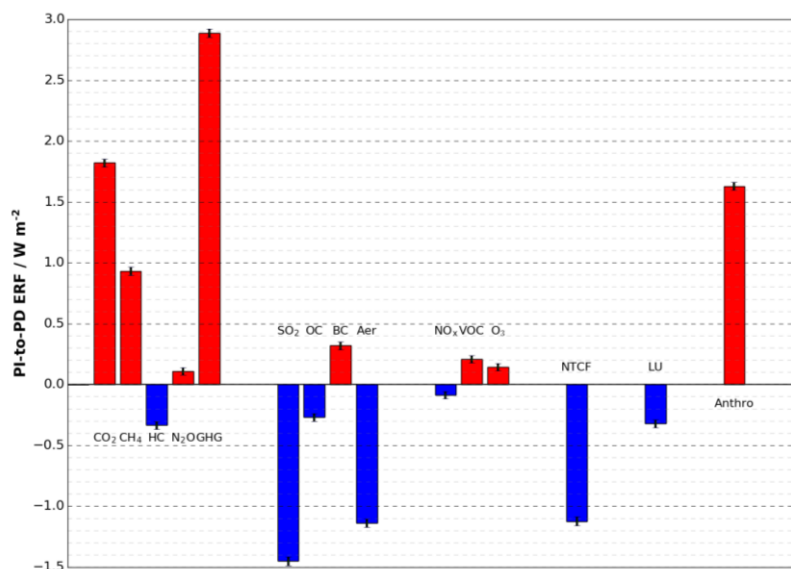
275

Figure 2: Bar chart showing global mean anthropogenic effective radiative forcings (ERFs) at the present day (Year 2014) relative to the pre-industrial (Year 1850), diagnosed from paired fixed SST timeslice simulations with an atmosphere-only configuration of UKESM1.

280 Figure 3 shows global distributions of the multi-annual mean PD ERFs from changes in GHGs, aerosols, tropospheric ozone (O_3) precursors, land use, and total anthropogenic sources since PI. It shows that the PD ERF from GHGs (Fig. 3a) is strongly positive everywhere although there is some evidence of negative forcing (up to -2 W m^{-2}) in the high latitudes, particularly in the southern hemisphere (SH). This is due to a negative ERF from the *piClim-HC* perturbation experiment (Table 3) which offsets the positive forcings from the other LLGHGs. Indeed, Morgenstern et al. (2019) found that the negative ERF from

285 ozone depletion and cloud feedbacks (including aerosol-mediated cloud feedbacks) offsets the direct positive ERF from the ozone-depleting substances (ODSs). The breakdown of the GHG forcing into its individual contributions will be discussed further in Sect. 3.2. The aerosol forcing (Figure 3b) is more spatially heterogeneous than the GHG forcing due to their shorter

lifetime. However, the distribution of the aerosol forcing is still largely negative everywhere, except for over bright surfaces and regions where the positive forcing from black carbon (BC) emissions outweighs the negative forcing from scattering

290 aerosols such as sulphate and organic carbon (OC). A breakdown of the aerosol forcing between constituents and between aerosol-radiation interactions (ari) and aerosol-cloud interactions (aci) will be presented and discussed in Sect. 3.3.

Figure 3c shows the global distribution of the PD ERF from emissions of tropospheric O_3 precursors. It shows that the forcing is spatially heterogeneous, has regions of both weak positive and weak negative contributions, but on a global mean basis is weakly positive (+0.15 W m^{-2}; Table 3) in comparison with other forcings (e.g. GHGs). Further analysis of the ERF from

295 tropospheric O_3 precursors and their contribution, along with methane (CH_4), to forcing by tropospheric O_3, can be found in Sect. 3.4. The distribution of the land use ERF (Fig. 3d) is spatially heterogeneous although much of the negative forcing is concentrated over the northern hemisphere (NH) continental regions (e.g. North America, South East Asia). Together with aerosols, their combined ERF outweighs the positive ERF from GHGs, leading to a negative total anthropogenic ERF over much of the NH continents (Fig. 3e). As was the case with the GHG forcing, the negative ERF over the SH high latitudes is

300 still evident in the total anthropogenic forcing.
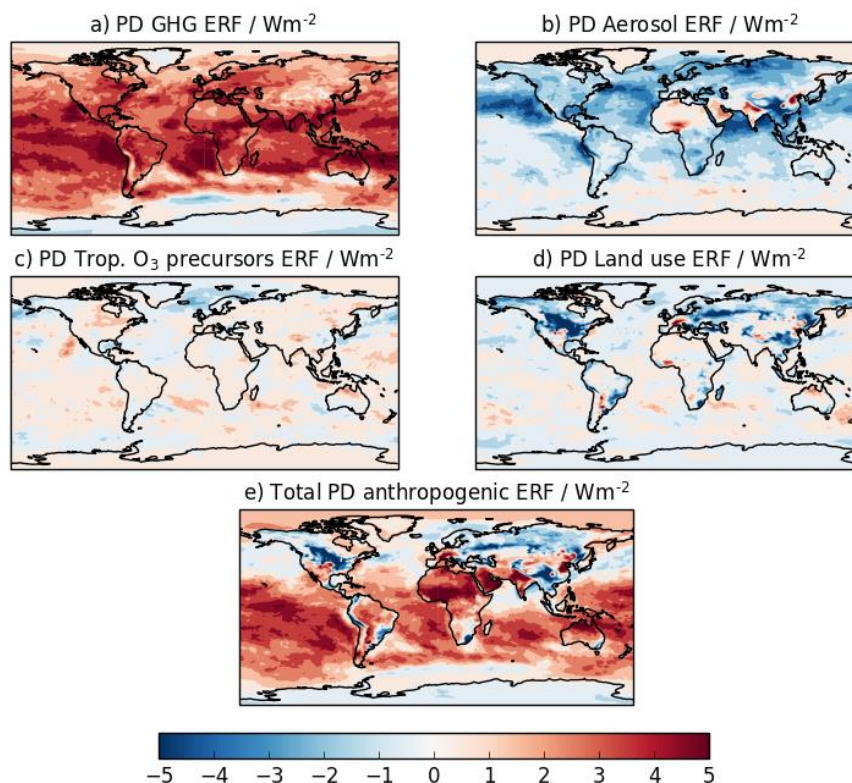
Figure 3: Geographical distribution of the multi-annual mean present-day (PD; Year 2014) effective radiative forcing (ERF) relative to the pre-industrial (PI; Year 1850) for (a) GHGs, (b) aerosols, (c) tropospheric ozone (O_3) precursors, (d) land use
305 **change, and (e) total anthropogenic, in W m^{-2}.**

As discussed in Sect. 2, the UKESM1 fixed SST experiments were run on multiple High Performance Computing (HPC) platforms. Despite statistical methods ensuring that the model is not scientifically different on the different HPC platforms, such duplicate experiments still produce slightly different results. This raises the question of the impact of such differences on the quantification of PD ERFs with UKESM1. To address this question, the experiments described in Table 2 were used to compare the difference in TOA radiative fluxes of equivalent realisation experiment pairs. The two-sample Kolmogorov–Smirnov test between the monthly TOA radiative fluxes from the realisation pairs (null hypothesis that the samples are drawn from the same distribution) shows that the TOA radiative fluxes between the two realisation pairs are statistically identical at a confidence level (α) of 5 %. Despite the fact that one cannot conclude that the distributions are identical, for each pair of experiments there is no evidence suggesting that the two distributions are different.

Pair	Differences in the TOA radiative fluxes (W m^{-2})						
	NET ERF	LWcs'	SWcs'	LW $\triangle$CRE'	SW $\triangle$CRE'	NETcs'	NET $\triangle$CRE'
piClim-SO2 R1 vs R2	+0.06 ±0.03	+0.02 0.02	+0.02 ±0.02	0.01 ±0.02	0.04 ±0.02	-0.008 ±0.02	+0.05 ±0.02
piClim-OC R1 vs R2	-0.03 ±0.03	-0.03 ±0.02	+0.007 ±0.01	-0.004 ±0.01	-0.004 ±0.02	-0.03 ±0.02	-0.008 ±0.02
piClim-NTCF R1 vs R2	0.00 ±0.00	0.00 ±0.00	0.00 ±0.00	0.00 ±0.00	0.00 ±0.00	0.00 ±0.00	0.00 ±0.00

Table 4: Differences in the TOA radiative fluxes (± standard error) in the clear-sky (CS) shortwave (SW), CS longwave (LW), and the SW and LW cloud radiative effect (CRE) at the present day (PD; Year 2014) between two realisations (R1 and R2) of the same perturbation experiment, in W m^{-2}.

4.2 Long-Lived Greenhouse Gases (LLGHGs)

4.2.1 Carbon Dioxide (CO$_2$)

Atmospheric carbon dioxide (CO$_2$) concentrations have risen from 284.3 to 397.5 ppm between 1850 and 2014 (Meinshausen et al., 2017) resulting in a global mean ERF of +1.83 ± 0.04 W m^{-2} (Table 3) and is the largest individual contribution to the total historical forcing. Myhre et al. (2013a) report a stratospherically adjusted radiative forcing (SARF) or RF of +1.82 ± 0.19 W m^{-2} for the period from 1750 to 2011 which, coincidentally, has a near identical rise in CO$_2$ of 113 ppm to that assessed here. An updated radiative forcing assessment based on line-by-line calculations (Etminan et al., 2016) increased SARF for 2015 relative to 1750 to 1.95 W m^{-2} but for a larger CO$_2$ rise of 121 ppm. Our ERF estimate for 2014 is, therefore, consistent with the SARF from line-by-line calculations and confirms that for CO$_2$, the SARF is a useful metric for evaluating the radiative

330 effects of increasing CO_2 (Smith et al., 2018). As expected for a GHG, the ERF is dominated by absorption in the clear-sky (CS) longwave (LW) (+1.56 ± 0.02 W m^{-2}) with additional CS shortwave (SW) forcing (+0.122 ± 0.02 W m^{-2}) coming from a rapid adjustment in snow-cover across the northern latitudes and a net cloud radiative effect (0.144 ± 0.03 W m^{-2}) from a reduction in cloud cover.

335 Rising atmospheric CO_2 also exerts an indirect forcing through rapid changes in plant stomatal conductance (Doutriaux-Boucher et al., 2009; Richardson et al., 2018) enhancing plant water use efficiency and reducing evapotranspiration leading to an increase in sensible heating at the surface and corresponding drying of the boundary layer and reduction in low-clouds. This mechanism is known as a physiological forcing. In UKESM1 (*piClim-CO2phys*; Table 3), this forcing is small for the PD (0.008 ± 0.04 W m^{-2}) but results from a balance between a negative CS LW component (-0.065 ± 0.03 W m^{-2}) associated with

340 surface warming and a positive SW cloud radiative effect (CRE) (0.112 ± 0.02 W m^{-2}) associated with a reduction in low-level cloud. The balance comes from smaller terms including a negative CS SW contribution from reduced water vapour. Previous Hadley Centre models at 4xCO_2 found a much larger effect: 1.1 W m^{-2} in HadCM3LC (Doutriaux-Boucher et al., 2009) and 0.25 W m^{-2} in HadGEM2-ES (Andrews et al., 2012b). Assuming the physiological effect scales linearly with atmospheric CO_2, we find that UKESM1 has a stronger CS LW component compared to HadGEM2-ES implying that UKESM1 has a more

345 pronounced surface warming adjustment associated with the physiological effect.

4.2.2 Nitrous Oxide (N_2O)

The global mean ERF due to changes in N_2O from PI (Year1850 value of 273 ppbv) to PD (Year 2014 value of 327 ppbv) is calculated as +0.13±0.03 W m^{-2} (Table 3), following the equations (6)-(8) described above. The predominant contribution to the N_2O ERF is the CS LW forcing (+0.25 ± 0.03 W m^{-2}), with a small and non-significant cancellation by the CS SW forcing

350 (-0.03 ± 0.02 Wm^{-2}); the net CS forcing sums up to +0.22 ± 0.03 W m^{-2}. The net cloud-radiative effect (CRE) forcing is -0.10 ± 0.03 W m^{-2}, with the SW and LW contributions of +0.03 ± 0.03 W m^{-2} and -0.13 ± 0.02 W m^{-2}, respectively. In comparison, the net ERF calculated here (+0.13 ± 0.03 W m^{-2}) is slightly lower than the SARF values of +0.17 ± 0.03 W m^{-2} from AR5 for 2011 (Myhre et al., 2013a) and of +0.18 W m^{-2} for 2014 based on the updated expression from Etminan et al. (2016). This is likely to be due to the effect of adjustments associated with changing N_2O that weren't considered as part of the SARF in AR5

355 (Myhre et al., 2013a) or Etminan et al. (2016), including O_3 depletion and fast cloud adjustments. Previously, Hansen et al. (2005) calculated an IRF and a SARF of 0.15 W m^{-2} due to the change in N_2O from 278 to 316 ppbv.

The global distribution of the individual components contributing to the N_2O ERF (Fig. 4) shows that the SW forcing is negligible under CS conditions and is largely made up of noise in cloudy conditions which might be due to an aerosol effect.

360 CS LW forcing is predominantly positive, due mainly to N_2O direct forcing. There are relatively large regional changes in the LW due to clouds leading to a significant net negative LW CRE of -0.13 W m^{-2}. The positive LW CRE over the southern high latitudes appears to be correlated to the change in total column ozone (TCO) and the shift of the surface wind shown in Fig. 5.

Zonal mean ozone (O_3) and temperature changes (Fig. 5) show the warming of the upper troposphere and lower stratosphere due to increased O_3 in that region and the cooling of the stratosphere due to O_3 depletion associated with the N_2O increase. As

365   a result, the atmospheric circulation has been modified, reflected in a shift of the upward velocity (w component of the wind) (Fig. 5d), which is correlated to the water content of the clouds. Such changes in clouds drive the LW forcing, which shows a pattern of significant regional changes with cancelling effects.
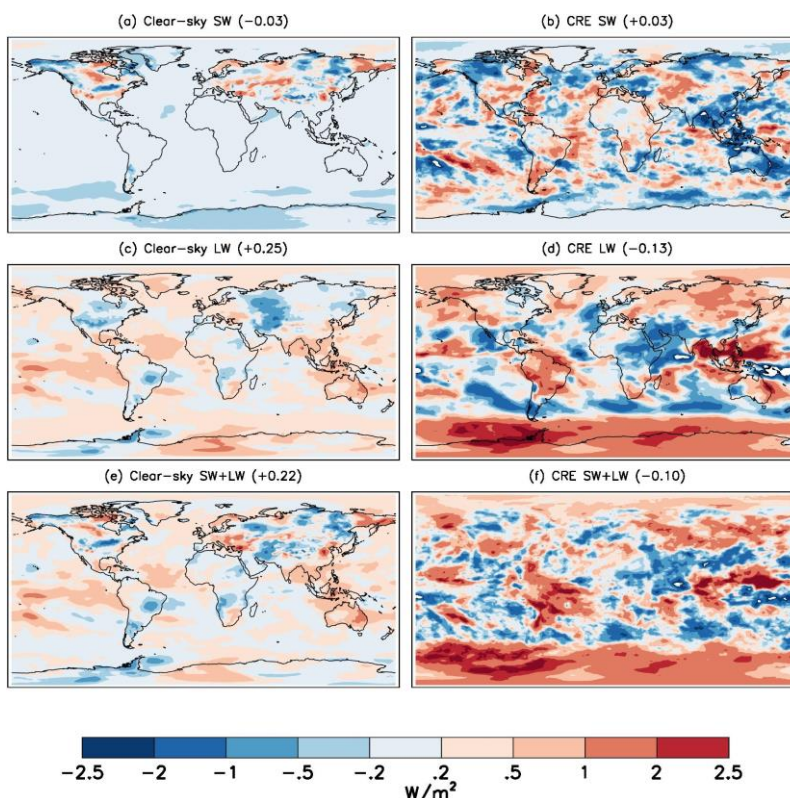
370   **Figure 4: Global distributions of the N_2O ERF at the top of atmosphere (TOA) for the present day (PD; Year 2014) relative to the pre-industrial (PI; Year 1850) i.e. *piClim-N2O* minus *piClim-Control*; (a) clear sky SW, (b) cloud-radiative effect (CRE) SW, (c) clear sky LW, (d) CRE LW, (e) net (SW+LW) for clear sky, and (f) net (SW+LW) CRE, in W m^{-2}.**

375   The change in TCO is largely negative due to a reduction in stratospheric O_3 (Fig. 5a). That would lead to a negative indirect forcing by O_3; indeed, the ERF calculated here is 0.05 W m^{-2} smaller than the direct N_2O forcing in AR5 (Myhre et al., 2013a). N_2O-induced O_3 depletion causes a strengthening of the Southern Annular Mode (evidenced in a poleward shift of the westerlies associated with the SAM). With that shift comes a redistribution of clouds with cloud structures also moving poleward. Tropical effects include a warming of the upper troposphere/lower stratosphere (UTLS) region associated with O_3

380   increases there, resulting in a regional suppression of convection and a reduction of associated LW radiation coming from
cloud tops.
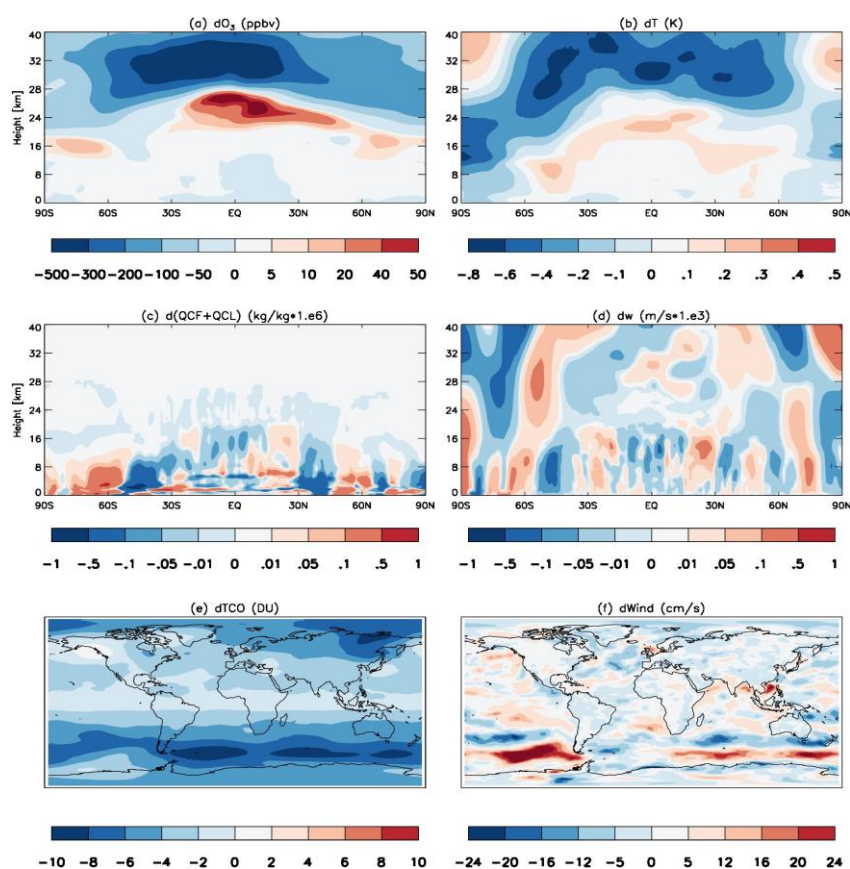
Figure 5: Global distribution of changes in zonal and annual mean a) O₃ (ppbv), b) temperature (K), c) cloud liquid water (qcl) and
385   **cloud frozen water (qcf), and d), vertical wind velocity, and global distributions of the multi-annual mean e) total column ozone**
(TCO) and f) near surface wind.

Prather and Hsu (2010) also noted that coupling of N₂O and methane (CH₄), via stratospheric O₃ depletion and photolysis, can
reduce the global warming potential (GWP) of N₂O by 5 %, based on PD concentrations. Here, the response of CH₄ is
390   constrained due to being concentration-driven. However, the whole-atmosphere CH₄ lifetime changes from 8.1 years in *piClim-*
control to 8.0 years in *piClim-N2O*, which would lead to a small offset to the N₂O ERF of 0.01 W m⁻² due to the direct radiative
effect of CH₄ if the model was emissions-driven; indirect CH₄ forcings (e.g. O₃) could enhance this offset even further
(O'Connor et al., 2019).

4.2.3 Halocarbons

395   The global multi-annual mean ERF from the PI to PD change in ozone depleting substances (ODSs) is quantified, using *piClim-HC* relative to *piClim-control*, as -0.33 ± 0.04 W m⁻². A quantitative and process-based understanding of why the ERF is negative, despite our understanding to date of the relative roles of ODSs and O_3 depletion in climate forcing, is presented in Morgenstern et al. (2019).

4.2.4 Methane (CH₄)

400   The global mean methane (CH_4) concentration changed from 808.3 ppbv in the PI (Year 1850) to 1831.5 ppbv in the PD (Year 2014), resulting in a PD ERF of +0.93±0.04 W m⁻² (Table 3; Fig. 6), where the 0.04 W m⁻² is the standard error following Forster et al. (2016). Most of the forcing (+0.73±0.02 W m⁻²) occurs in the CS LW, with an additional positive contribution (+0.12±0.01 W m⁻²) from the CS SW, consistent with the growing recognition of the importance of the SW absorption bands in CH_4 forcing (Collins et al., 2006; Li et al., 2010; Etminan et al., 2016). There are additional SW and LW contributions from

405   the cloud radiative effect (CRE) but these largely cancel out, leading to a small net positive forcing (+0.08 ± 0.03 W m⁻²) in addition to the net CS forcing (+0.85±0.03 W m⁻²). Estimates of the direct CH_4 ERF at the PD from HadGEM2 model simulations (Andrews, 2014) and the updated RF expression for CH_4 based on line-by-line calculations (Etminan et al., 2016) are of the order of 0.50-0.56 W m⁻². But the forcing calculated here is higher by more than 0.4 W m⁻². However, it is consistent with other studies (e.g. Hansen et al., 2005; Shindell et al., 2009; Myhre et al., 2013a), who concluded that the total climate

410   forcing by CH_4 is almost double that of the direct forcing due to indirect effects. The UKESM1 estimate is also larger than the +0.69 W m⁻² radiative impact of an increase in CH_4 concentration of 1800 ppbv above present-day levels quantified by Winterstein et al. (2019) with the ECHAM/MESSy Atmospheric Chemistry (EMAC) coupled model. Although the Winterstein et al. (2019) estimate included indirect forcings from O_3 and stratospheric water vapour (SWV), their direct CH_4 forcing in the LW is low relative to other models (Lohmann et al., 2010). The relative contributions of the direct and indirect forcings to the

415   total CH_4 ERF quantified here and an emissions-based perspective of the CH_4 forcing can be found in O'Connor et al. (2019).

4.2.5 Total Greenhouse Gases (GHG)

The major driver of anthropogenic climate change is greenhouse gases (GHGs), which is offset by aerosols (Myhre et al., 2013a). Therefore, the total greenhouse ERF and the total aerosol ERF are key metrics in understanding observed and modelled changes in the climate system since the PI. As a result, a separate timeslice simulation with all GHGs (*piClim-GHG*; Table 1)

420   was conducted following the RFMIP protocol (Pincus et al., 2016).
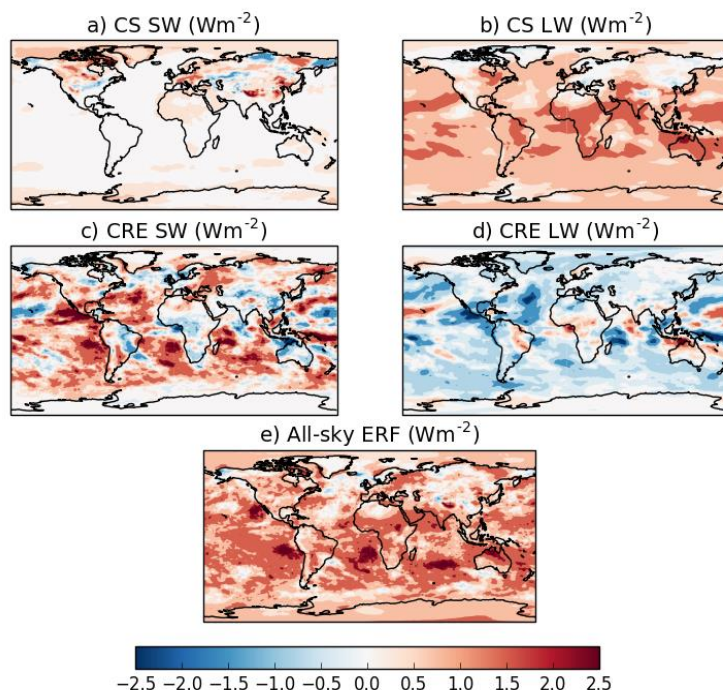
Figure 6: Global distribution of the components of the PD (Year 2014) methane ERF relative to PI (Year 1850): a) Clear-sky (CS) shortwave (SW), b) CS longwave (LW), and the cloud radiative effect (CRE) in the c) SW and d) LW, and the all-sky ERF in e) calculated using Equations (6)-(8) according to Ghan (2013). Forcings in W m⁻².

The UKESM1 *piClim-GHG* experiment leads to an ERF of 2.89 ± 0.04 W m⁻² (Table 3), which is dominated by a positive CS LW contribution (3.08 W m⁻²) that is partially offset by a negative CS SW component (-0.16 W m⁻²). There are significant positive and negative contributions from the CRE in the SW and LW but these largely cancel out and contribute little (-0.01 W m⁻²) to the total ERF (Table 3). This PD GHG ERF is lower than the ERF of 3.09 W m⁻² estimated from the physical model HadGEM3-GC3.1 (Andrews et al., 2019). Part of this discrepancy may be due to the inclusion in UKESM1 of indirect forcings by O_3 and/or aerosols from O_3-depleting substances (Morgenstern et al., 2019) and CH_4 (O'Connor et al., 2019), for example. The UKESM1 1850-2014 estimate, however, is consistent with the AR5 year-2011 SARF estimate of 2.82 W m⁻². The latter estimate has been adjusted to an 1850 baseline from 1750, and taking stratospheric O_3 depletion, CH_4-driven SWV, and half of the tropospheric O_3 forcing (based on the attribution by Stevenson et al., 2013) into account, although some GHG concentrations (e.g. CH_4) have increased between 2011 and 2014 (Nisbet et al., 2016) while others (e.g. ODSs) have declined (Engel et al., 2018).

Although, in principle, one could use the combination of GHG simulations to test for linearity, this isn't feasible here; *piClim-GHG* perturbs non O_3-depleting halocarbons whereas *piClim-HC* does not. However, there is a discrepancy in ERF of 0.35 W

m^{-2} between *piClim-GHG* and the sum of the individual GHG simulations which cannot be fully accounted for by the small positive RF from non O$_3$-depleting halocarbons (HFCs, PFCs, SF6) of 0.02 W m^{-2} at 2011 (Myhre et al., 2013a). This suggests that there is a potential non-linearity in the GHG forcing, perhaps involving O$_3$ chemistry and aerosol-mediated cloud feedbacks, which may warrant further investigation.

4.3 Aerosols and Aerosol Precursors

Figure 7a summarizes the results from the anthropogenic aerosol experiments, including a breakdown of the ERF into instantaneous radiative forcing (IRF) and rapid adjustments (RA) for each of the anthropogenic aerosol experiments (*piClim-SO2*, *piClim-OC*, *piClim-BC*, and *piClim-aer*). The IRF was calculated using the double-call system where aerosol-radiation interactions (ari) (i.e. scattering and absorption) are withdrawn from the second call to the radiation scheme, as in Ghan et al. (2012). The rapid adjustments (RA) have then been derived as the residual between the ERF and IRF and includes all aerosol-induced changes in cloud radiative effects.

Uncertainties in aerosol ERF are likely to be driven by uncertainties in the PI aerosol state (Carslaw et al., 2013) as well as the oxidising capacity of the atmosphere (Karset et al., 2018). The additional interactive sources of natural aerosol in UKESM1 for marine dimethyl sulphide (DMS), terrestrial and marine biogenic sources, along with the inclusion of a fully interactive chemistry scheme (Archibald et al., 2019) are generally found to improve the evaluation of PD aerosol in UKESM1 (Mulcahy et al., 2019). This provides some confidence in the underlying physical processes driving the PI aerosol state in this model.

The total anthropogenic aerosol ERF evaluated from the "all" (*piClim-aer*) experiment is -1.13 W m^{-2}, which is almost identical to the ERF of -1.10 W m^{-2} from the physical model HadGEM3-GA7.1 (Andrews et al., 2019) and slightly lower in magnitude than the ERF of -1.45 W m^{-2} derived from HadGEM3-GA7.1 with CMIP5 emissions (Mulcahy et al., 2018). The estimate fits well within the likely range of -1.60 to -0.65 W m^{-2} (16-84 % confidence level) provided by a recent major assessment of PI to PD aerosol ERF (Bellouin et al., 2019) and the -1.5 to -0.4 W m^{-2} likely range previously assessed by AR5 (Myhre et al., 2013a). The annual-mean global distribution of aerosol ERF, IRF and aci are shown in Fig. 8. The total aerosol ERF (Fig. 8a) is negative over most regions, and is strongest over the cloudy ocean regions of the Northern Hemisphere where the forcing is dominated by the RA term (Fig. 7a) driven by aerosol-cloud interactions (aci) (Fig. 8c). Some areas of Asia and North Africa have positive total aerosol ERF due to BC-rich aerosol loadings that give locally positive aerosol IRF (Fig. 8b). However, globally, the IRF is rather small and negative (-0.16 W m^{-2}) (Fig. 7a) due to scattering by sulphate and OC that is partially offset by absorption from BC.
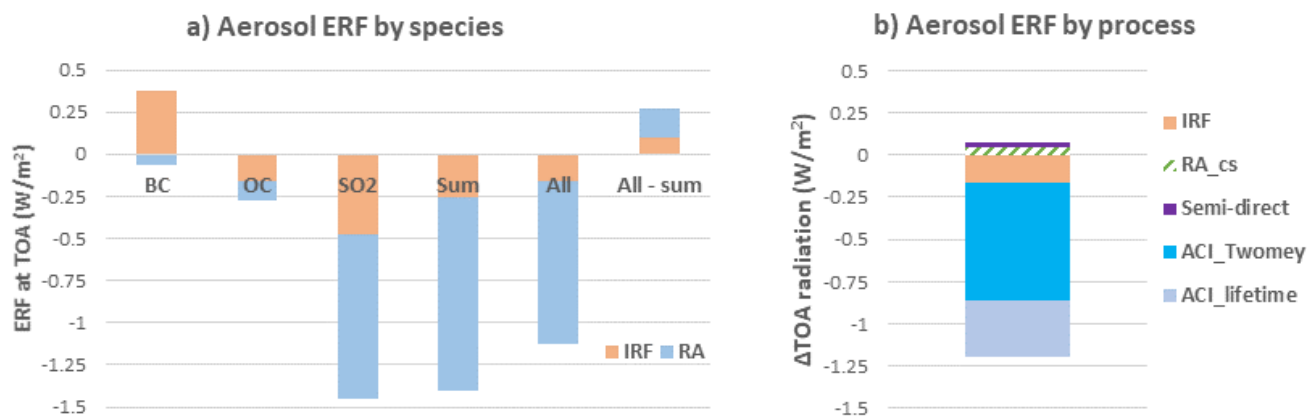
Figure 7: Aerosol ERF at TOA for the period 1850 - 2014, broken down by species and process. (a) Results are from *piClim-BC*, *piClim-OC*, *piClim-SO2*, from summing those three experiments (Sum), and from *piClim-aer* (All aerosol). (b) Total aerosol ERF decomposed into various contributing processes from the *piClim-aer* and accompanying sensitivity tests: IRF = instantaneous
475 **radiative forcing, RA = rapid adjustments, ACI = aerosol-cloud interactions, RA_cs = clear-sky rapid adjustments (e.g. surface albedo, atmospheric temperature and water vapour).**

The SO$_2$ emissions are the largest individual contributor to the aerosol ERF and have a strong RA (aci) component leading to an SO$_2$ (equivalent to sulphate) ERF of -1.45 W m^{-2} (Table 3, Fig. 7a). The IRF component of the sulphate ERF is -0.48 W m^{-2}

480 , which agrees well with the best estimate from AR5 (-0.40 ± 0.2 W m^{-2}) and from AEROCOM II (-0.58 to -0.11 W m^{-2}) (Myhre et al., 2013b). The BC ERF was +0.32 W m^{-2}, coming mostly from the IRF (0.38 W m^{-2}) and small negative offset of -0.06 W m^{-2} from rapid adjustments. As noted in Johnson et al. (2019), BC absorption leads to strong cloud adjustments but the SW and LW components of these almost cancel in HadGEM3-GA7.1 and UKESM1 (see Table 3). This contrasts with many other models where the combination of low cloud enhancements and reductions in upper-level cloud typically result in

485 more substantial negative adjustments, making the BC ERF on average about half the magnitude of the IRF (Stjern et al., 2017). The BC ERF given by UKESM1 is however well within the range assessed by AR5 (0.05 - 0.8 W m^{-2}), which took into consideration the possibility that BC emissions and/or absorption efficiency were underestimated in CMIP5 models (Bond et al., 2013). The anthropogenic emissions of BC were specified as 5 Tg yr^{-1} in CMIP5 (Year 2000 as PD) but have increased to 8 Tg yr^{-1} in CMIP6 (Year 2014 as PD). With CMIP5 emissions, the BC ERF from HadGEM3-GA7.1 was found to be 0.17

490 W m^{-2} (Johnson et al., 2019) and is comparable to direct BC forcing from other CMIP5 model estimates (Myhre et al., 2013a). It is worth noting that the aerosol absorption was in fairly good agreement with AERONET observations in HadGEM3-GA7.1 simulations that used the CMIP5 emission set (Mulcahy et al., 2018). The slightly higher CMIP6-based estimate of 0.32 W m^{-2} provided in the present study could therefore be an overestimate, although this is difficult to judge given the uncertainties in comparing models with absorption measurements. It is also worth noting that BC forcing can have proportionately larger

495 impacts on surface radiation, precipitation and regional circulation due to the localised absorption of solar radiation in the atmosphere.
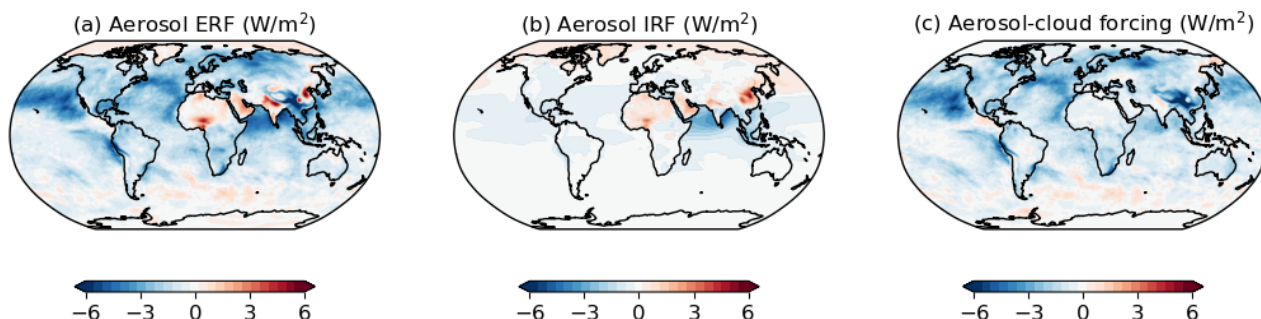
Figure 8: Multi-annual mean changes in TOA net radiation from piClim-aer (all anthropogenic aerosols), including (a) The ERF, (b) the IRF, (c) aerosol-cloud forcing due to aerosol-cloud interactions and the semi-direct aerosol effect.

500

The PD OC ERF relative to PI is -0.27 W m^{-2}, with -0.16 W m^{-2} from the IRF and -0.11 Wm^{-2} from RA (Fig. 7a, Table 3). The OC IRF estimate agrees well with AR5 that assessed the RF of primary and secondary OC to be -0.12 W m^{-2} (-0.4 to +0.1). Note that OC is non-absorbing in UKESM1 and, as such, neglects the role of brown carbon. This potentially misses a small positive contribution to the aerosol forcing (e.g. Feng et al., 2013), although biomass burning emissions are the dominant

505 global source of brown carbon and these do not change significantly from 1850 to 2014 (Saleh et al., 2014). The contribution of brown carbon to aerosol ERF is, therefore, likely to be small compared to the overall uncertainty in modelling aerosol absorption by BC (Bond et al., 2013). Nitrate aerosols are also not represented in HadGEM3-GA7.1 (Mulcahy et al., 2018; Walters et al., 2019) or UKESM1 (Sellar et al., 2019; Mulcahy et al., 2019) so the ERF associated with ammonia (NH$_3$) emissions could not be evaluated here. The total aerosol ERF in UKESM1 would presumably be more strongly negative if the

510 role of nitrate aerosol was included (e.g. Bellouin et al., 2011) and this should be borne in mind when making comparisons with other models or estimates based on observational constraints.

The "all" aerosol forcing experiment combines the increases in BC, OC and SO$_2$ emissions together in one simulation, and interestingly, the ERF is 0.27 Wm^{-2} weaker (less negative) than the sum of the ERFs from the experiments that perturb those

515 emissions separately. The main reasons for this lack of linearity are: (i) Cloud droplet numbers do not increase linearly with aerosol loading (e.g. Jones et al., 1994) and begin to saturate in the "all" experiment (*piClim-aer*), which means OC and BC emissions no longer contribute significantly to aci once co-emitted with year-2014 levels of SO$_2$. (ii) The absorption of upwelling shortwave radiation by BC is enhanced by increases in aerosol scattering and cloud brightness due to aci, making the IRF less negative in the "all" experiment.

520

To further understand which processes contribute most to total aerosol ERF, a series of additional sensitivity experiments were conducted with aci processes selectively disabled. In these tests, the cloud droplet number concentrations (CDNCs) used for

the calculation of cloud droplet effective radius (Reff) and/or autoconversion were prescribed via a 3D monthly-mean PI climatology constructed from the final 30 years of the *piClim-control* simulation. The resulting global-mean ERFs are

525   summarized in Fig. 7b. In one pair of simulations, CDNCs were prescribed for the Reff calculation to disable the so-called Twomey effect (Twomey, 1977). By comparison with the main *piClim-aer* experiment, this indicated a Twomey effect (ACI_Twomey) of -0.73 W m^{-2}. A similar pair with CDNCs prescribed only for the autoconversion process led to an estimate of -0.34 W m^{-2} for the cloud lifetime effect (ACI_lifetime) (Albrecht, 1989). By prescribing CDNCs for both Reff and autoconversion both microphysical aci processes are disabled and only aerosol-radiation interactions (ari) are included. A pair

530   of simulations with this setup provided an estimate for ERF$_{ari}$ of -0.14 W m^{-2}. The change in CRE in the ari-only experiment was only +0.04 W m^{-2}, which is not statistically significant at the 95% confidence level and indicates that the semi-direct aerosol effect is small or approximately neutral in this model. To complete the breakdown, the method in Ghan (2013) was further used to derive the contribution from changes in "clean" (aerosol-free) CS radiation (RA_cs). This term was found to be +0.05 W m^{-2}, and arises due to changes in surface albedo and atmospheric temperature and humidity. This overall

535   breakdown suggests an aerosol-cloud forcing of -1.03 W m^{-2}, with a roughly 70/30 split between the Twomey effect and aerosol effects on cloud cover and water content (lifetime & semi-direct effects).

The estimated aerosol-cloud forcing sits well within the 90 % likelihood ranges assessed by AR5 (-1.2 to 0.0 W m^{-2}) and Bellouin et al. (2019) (-2.0 to -0.35 W m^{-2}), although these broad ranges reflect the large uncertainties involved in constraining

540   global estimates with observations (e.g. Ghan et al., 2016). At present there are no definitive constraints on the proportionate contributions that the Twomey and other aerosol-cloud effects make towards the total aerosol-cloud forcing, but recent observational evidence (Malavelle et al., 2017; Toll et al., 2017) supports the supposition that the Twomey effect is the dominant process and that some models overestimate cloud lifetime effects. Toll et al. (2017) indicated that HadGEM3 can indeed overestimate the cloud lifetime effect in marine stratocumulus, whereas Mallavelle et al. (2017) found HadGEM3 to

545   correctly simulate only weak cloud lifetime effects for mixed cloud regimes over the North Atlantic. The UKESM1 estimate of ERF$_{ari}$ of -0.14 W m^{-2} is within the 5-95% confidence range (-0.45 +/- 0.5 W m^{-2}) from AR5 but slightly weaker than the range of values estimated by Bellouin et al. (2019) (-0.60 to -0.25 W m^{-2}). Possible reasons include the lack of nitrate, the relatively strong BC forcing compared to CMIP5 models, and a slight underestimation of aerosol optical depth in PD simulations relative to some satellite products (Mulcahy et al., 2019).

550   **4.4 Tropospheric ozone (O$_3$) precursor gases**

The global mean ERF from emissions of tropospheric ozone (O$_3$) precursors is weakly positive (+0.15 W m^{-2}; Table 3), although spatially heterogeneous, with regions of positive and negative forcing. Tropospheric O$_3$ precursor emissions affect the ERF both through changes to tropospheric O$_3$, a GHG, and by changing tropospheric oxidants such as OH, which in turn affect aerosols (Karset et al., 2018) and CH$_4$. Here, we explore the composition and forcings resulting from O$_3$ precursor

555   emissions changes between the PI and PD by comparing the *piClim-O3* simulation with *piClim-control* and the separate effects

of nitrogen oxide (NOx) and volatile organic compound (VOC)/carbon monoxide (CO) emissions changes using the *piClim-NOx* and *piClim-VOC* simulations, respectively.
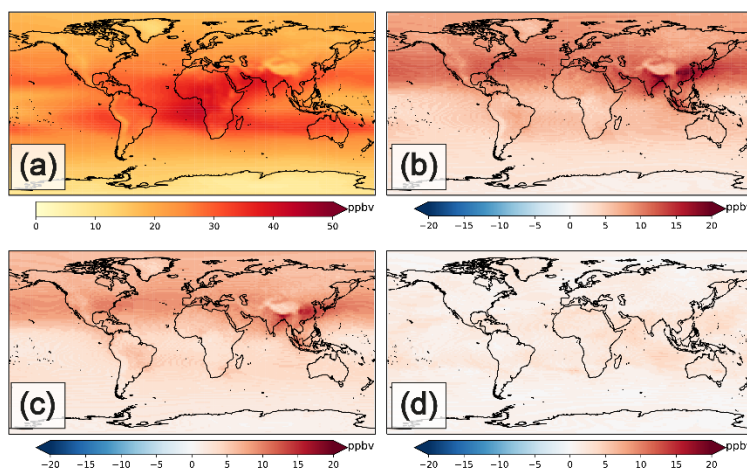
Figure 9: Global distributions of the multi-annual distributions of tropospheric O_3 column (a) in *piClim-control*. Differences with respect to *piClim-control* from *piClim-O3*, *piClim-NOx* and *piClim-VOC* can be seen in panels b), c) and d), respectively.

4.4.1 Tropospheric Ozone (O_3) Changes

The multi-annual mean tropospheric O_3 column for the *piClim-control* simulation, and tropospheric O_3 column differences between *piClim-control* and the *piClim-O3*, *piClim-NOx* and *piClim-VOC* simulations are shown in Fig. 9. O_3 levels in the troposphere are the result of competing production and loss processes. Production occurs in the presence of NOx and VOC/CO, with most regions of the troposphere being NOx-limited. PI tropospheric column O_3 values (Fig. 9a) show maxima over central Africa and the South Pacific, the result of relatively large emissions of NOx from soil, biomass burning and lightning in this region, and minima over regions remote from NOx sources, such as the Western Pacific (where O_3 loss is efficient) (Young et al., 2018). O_3 columns are also low over regions of high surface elevation where the atmospheric column is shallower.

Tropospheric O_3 column values increase when the model is perturbed with the larger PD O_3 precursor emissions in *piClim-O3*, with the largest increases in the northern hemisphere, particularly in southern and eastern Asia. The tropospheric O_3 burden increases from 280.1 Tg in *piClim-control* to 356.1 Tg in *piClim-O3*. As can be seen in Fig. 9, the dominant driver of these changes is increased NOx emissions, and there is a similar pattern of changes in the *piClim-O3* and *piClim-NOx* simulations, although the change in O_3 is smaller in the latter; the burden in *piClim-NOx* is 335.7 Tg. Small increases in O_3 are observed in *piClim-VOC*, with some hotspots in regions such as South East Asia and the O_3 burden increases to 297.2 Tg.

The tropospheric O_3 column difference between *piClim-O3* and *piClim-control* of 76.0 Tg is slightly larger than the sum of the individual O_3 burden changes in *piClim-NOx* (55.6 Tg) and *piClim-VOC* (17.1 Tg) which total 72.7 Tg. However, these

580   differences due to the non-linear nature of tropospheric chemistry are small, on the order of < 10 %. Similar behaviour is seen in the patterns of the tropospheric O_3 column difference between *piClim-control* and other experiments.

4.4.2 Tropospheric Ozone (O_3) Radiative Forcing

As seen from earlier sections, it can be difficult to compare ERFs estimated from these experiments against estimates of RF (e.g. Stevenson et al., 2013; Myhre et al., 2013a), due to the inclusion of indirect forcings and/or rapid adjustments other than the stratospheric temperature adjustment although Shindell et al. (2013b) noted that for O_3, SARF and ERF estimates are
585   comparable. Nevertheless, in order to compare against Stevenson et al. (2013), we estimate SARF for the tropospheric O_3 precursor experiments by adopting a radiative kernel approach (e.g. Soden et al., 2008). This involves applying the tropospheric O_3 radiative kernel from Rap et al. (2015) to the diagnosed change in tropospheric O_3 (using the 150 ppbv O_3 isoline in *piClim-control* as a tropospheric mask, as used in Young et al., 2013, Stevenson et al., 2013, and Rap et al., 2015) to calculate a stratospherically-adjusted radiative forcing (SARF) or RF. In this way, we can directly compare against the best estimate of
590   the 1850-2010 tropospheric O_3 RF of 364 mW m^{-2} by Stevenson et al. (2013) and quantify the contribution of different tropospheric O_3 precursors (including methane) to the PI-to-PD change in tropospheric O_3 and its RF. We can also compare with more recent estimates from Checa-Garcier et al. (2018) and Yeung et al. (2019).

Figure 10 shows the global distribution of the PD tropospheric O_3 RF from *piClim-CH4*, *piClim-NOx*, and *piClim-VOC*
595   experiments and their sum using the kernel approach. It shows that the tropospheric O_3 RF is strongest over the northern hemisphere tropics and weakest over the southern hemisphere high latitudes. The strongest RF occurs in regions of warm surface temperatures and high albedo, coinciding with the largest tropospheric O_3 change (Shindell et al., 2013a). As was the case in Stevenson et al. (2013), the forcing is weaker over regions of high altitude (e.g. Tibetan Plateau) due to there being less O_3 column aloft to absorb in the longwave (LW). On a global annual mean basis, the tropospheric O_3 RF from the kernel
600   approach is 407 mW m^{-2}, higher than the best estimate of Stevenson et al. (2013) by approximately 11 %. However, the Edwards and Slingo (1996) radiation scheme, which was used to generate the kernel, can lead to forcing estimates that are higher than other comparable radiation schemes (Stevenson et al., 2013). Other potential differences are due to experimental setup. The Atmospheric Chemistry and Climate Model Intercomparison Project (ACCMIP; Lamarque et al., 2013) simulations were timeslices and included historical climate change although Stevenson et al. (2013) found that to have a minimal impact
605   on the RF. More importantly, the increase in tropospheric O_3 at the PD (and its resulting RF) were offset by decreases due to the downward transport of O_3-depleted stratospheric air (e.g. Shindell et al., 2013a). Applying the kernel method to the diagnosed decrease in tropospheric O_3 from the *piClim-HC* experiment (Sect. 3.2.3), we find a RF offset of -101 mW m^{-2}, larger in magnitude by nearly a factor of 2 than the estimates from Søvde et al. (2011) and Shindell et al. (2013a), thus reducing our original estimate to 306 mW m^{-2}. This revised estimate is 15 % lower than the Stevenson et al. (2013) best estimate.
610   However, it is consistent with a number of other estimates: the CMIP6 historical O_3 dataset (312 mW m^{-2} from Checa-Garcia et al., 2018), a recent study in which observational isotopic data was used as a constraint on historical increases in tropospheric

O_3 (330 mW m^{-2} derived from the GEOSChem model in Yeung et al., 2019), and a parametric model based on multi-model source-receptor relationships (290 ± 3 mW m^{-2} from Turnock et al., 2019).
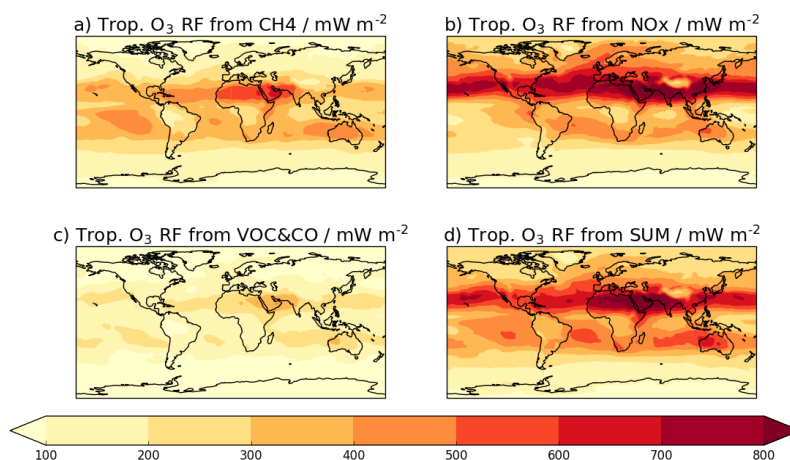
Figure 10: Global distribution of PD tropospheric O₃ RF diagnosed from a) *piclim-CH4*, b) *piClim-NOX*, c) *piClim-VOC*, and d) their sum relative to *piClim-control*, based on the diagnosed change in tropospheric O₃ and the tropospheric O₃ radiative kernel of Rap et al. (2015).

In considering the attribution of the tropospheric O_3 RF to its precursors, initial estimates (Fig. 10; Table 5) indicate that it is predominantly NOx driven (48 %), followed by CH_4 (34 %), with the smallest contribution from VOCs and CO (18 %). This is qualitatively consistent with Stevenson et al. (2013). However, as outlined in detail in that paper, these estimates do not take account of potential CH_4 (and O_3) changes that would occur were these experiments driven by CH_4 emissions rather than concentrations (e.g. Shindell et al., 2005). Taking the same approach as Stevenson et al. (2013), we calculate an equilibrium CH_4 concentration for the perturbation experiments, using the total CH_4 lifetime relative to *piClim-control* based on the following (Fiore et al., 2009):

$$[CH_4]_{piClim-X} = [CH_4]_{piClim-control} * \left(\frac{\tau_{piClim-X}}{\tau_{piClim-control}} \right)^f \quad , \qquad (9)$$

where $[CH_4]_{piClim-X}$ is the global mean equilibrium CH_4 concentrations in the *piClim-X* experiments, $[CH_4]_{piClim-control}$ is the prescribed global mean CH_4 concentration in *piClim-control*, $\tau_{piClim-control}$ and $\tau_{piClim-X}$ are the whole-atmosphere CH_4 lifetimes in the *piClim-control* and *piClim-X* perturbation experiments, respectively. The CH_4-OH feedback factor (Prather, 1996) is denoted by *f* and is defined as:

635
$$f = \frac{1}{1-s} \qquad , \qquad (10)$$

where s, called the sensitivity coefficient, is calculated from the following:

$$s = \frac{\delta ln\, \tau}{\delta\, ln\, [CH_4]} \qquad . \qquad (11)$$

640

Using the whole-atmosphere CH_4 burden and its removal by OH, the whole-atmosphere CH_4 lifetime is 8.1 and 9.8 years in *piClim-control* and *piClim-CH4,* respectively, when adjusted for stratospheric removal (160 yr lifetime) and soil uptake (120 yr lifetime). From Eqns. (10) and (11), the UKESM1 feedback factor f is 1.28, consistent with the range of other estimates (Prather et al., 2001; Shindell et al., 2005; Fiore et al., 2009; Stevenson et al., 2013; Voulgarakis et al., 2013; Turnock et al.,

645 2018) and within 5 % of the observationally constrained best estimate of 1.34 (Holmes et al., 2013). Then, using the difference between the global mean prescribed and equilibrium surface CH_4 concentrations, we calculate the additional tropospheric O_3 forcing in the *piClim-CH4*, *piClim-NOx* and *piClim-VOC* experiments by applying the tropospheric O_3 radiative kernel (Rap et al., 2015) to the O_3 response derived from scaling the (*piClim-CH4* minus *piClim-control*) O_3 response based on the relationship in Turnock et al. (2018); this additional contribution to the tropospheric O_3 RF is shown in Table 5.

650

Changing from a concentration-based perspective to an emissions-based view increases the tropospheric O_3 RF between PI and PD from 407 to 461 mW m^{-2} (an increase of 13 %), which agrees better with Stevenson et al. (2013) once the offset by O_3 depletion is accounted for (-101 mW m^{-2}). It also changes the relative contributions of the different tropospheric O_3 precursors. The contribution of CH_4 now dominates (45 %), with NOx playing a smaller role (36 %), while the contribution from VOC/CO

655 emission increases is relatively unchanged (19 %). These emissions-based contributions are well within the spread of estimates from Stevenson et al. (2013) who quantified contributions from 6 of the ACCMIP models: CH_4 (44 ± 12 %), NOx (31 ± 9 %), and VOC/CO (25 ± 3 %) although there are some differences with Shindell et al. (2005) and Shindell et al. (2009). In both Shindell et al. studies, the contribution from NOx is lower at 15 ± 8 and 11 %. The difference may be due to the strong sensitivity of the CH_4 lifetime to NOx in the GISS model compared with other models (Wild et al., 2019) and/or could be due

660 to differences in VOC chemistry; Archibald et al. (2010) showed that the response of OH to increasing NOx strongly depends on the treatment of VOC chemistry. Nevertheless, this approach demonstrates the importance of an emissions-based view of climate forcing and is more directly relevant to policy makers than a concentration-based view (Shindell et al., 2005; Shindell et al., 2009).

Pair	Trop. O_3 RF / mW m^{-2}	Equilibrium CH_4 concentration / ppbv	Additional Trop. O_3 RF from ΔCH_4 / mW m^{-2}	Total Trop. O_3 RF / mW m^{-2}
piClim-NOx minus *piClim-control*	196	563.4	-31	165
piClim-VOC minus *piClim-control*	73	927.8	15	88
piClim-CH4 minus *piClim-control*	138	2364.9	70	208
SUM minus *piClim-Control*	407	N/A	N/A	461

665

Table 5: Equilibrium CH_4 concentrations in the different perturbation experiments (*piClim-NOx*, *piClim-VOC*, and *piClim-CH4*) relative to the pre-industrial control (*piClim-control*), and the resulting additional tropospheric O_3 radiative forcing.

4.4.3 ERF: Role of Other Oxidants and Aerosols

In addition to O_3 being a GHG, it is also important for secondary aerosol formation along with other oxidants: hydroxyl (OH),

670 hydrogen peroxide (H_2O_2) and nitrate (NO_3). The OH radical in UKESM1 (Sellar et al., 2019) is involved in aerosol nucleation of gas-phase sulphuric acid (H_2SO_4) via the reaction with sulphur dioxide (SO_2), leading to new particle formation (Mulcahy et al., 2019). O_3 and H_2O_2 are important for SO_2 oxidation in cloud and aerosol droplets, creating sulphate aerosol mass but not number. Likewise, oxidation of monoterpenes by O_3, OH, and NO_3 determines the rate of formation of secondary organic aerosol (SOA) in UKESM1 (Kelly et al., 2018; Mulcahy et al., 2019) although it doesn't lead to new particle formation. Thus,

675 sulphate aerosol alone, through changes in O_3, OH, and H_2O_2, has potentially important impacts on cloud and aerosol radiative properties. Indeed, Karset et al. (2018) found that PD to PI oxidant changes in the CAM5.3-Oslo model alter the relative importance of different chemical reactions, leading to changes in aerosol size distribution, cloud condensation nuclei (CCN), and the PD aerosol ERF.

680 Figure 11 (bottom row) shows a global distribution of OH in *piClim-control* and changes in the perturbation experiments relative to *piClim-control*. The *piClim-control* experiment shows an OH maximum in the equatorial humid regions, where photolytic production of OH from excited oxygen atoms (O^1D) and water vapour (H_2O) is at a maximum. In *piClim-O3*, OH increases throughout the northern hemisphere due to increases in O_3, which is the precursor of O^1D. These increases in OH are driven largely by increases in NOx. However, the *piClim-VOC* experiment shows the opposite behaviour - while VOC and

685 carbon monoxide (CO) emissions increases serve to increase O_3, they also remove OH via direct reaction with OH. This latter effect outweighs the small increase in O_3 in *piClim-VOC* and there are large decreases in OH throughout the troposphere.

When OH is lower, we anticipate a decrease in the number of CCN, a decrease in cloud droplet number concentration (CDNC), leading to larger cloud droplets (Twomey, 1977), and an increase in the effective radius of cloud droplets (Reff). The middle

690   rows of Fig. 11 show these effects at work. In *piClim-control*, the distribution of CDNC shows large values in equatorial regions, in regions of continental outflow and regions of deep convection. Large increases in CDNC are seen in *piClim-NOx*, with large decreases in *piClim-VOC*. These results reflect the changes in OH in these experiments - increases in OH lead to increases in CDNC, and vice versa, but it should be noted that the effect of OH on CDNC is seen over a larger region downwind, particularly in East Asia and over the North Atlantic. The impact of NOx emissions appears to dominate, given

695   the similarity between *piClim-O3* and *piClim-NOx*, but the eastern Pacific is a region where all experiments show a decrease in CDNC.
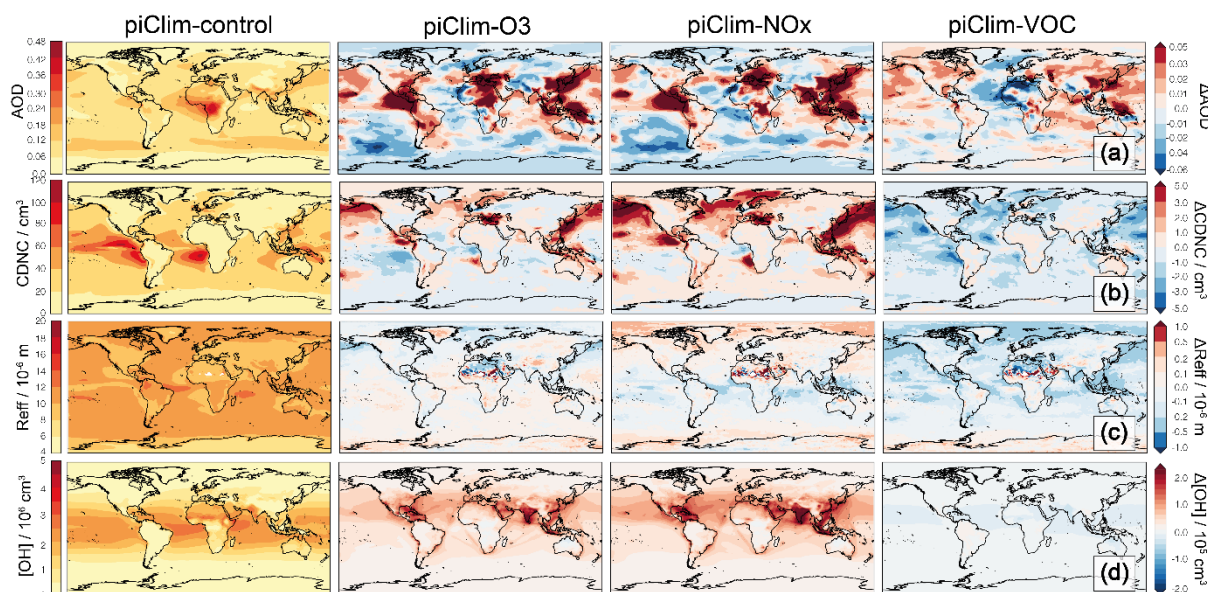
Figure 11: Global distributions of the multi-annual distributions of AOD (row (a); left column), cloud droplet number concentration
700   **(CDNC; cm⁻³) at 1km (row (b); left column), cloud droplet effective radius (Reff; μm) at 1km (row (c); left column) and OH number concentration (cm⁻³) at 1km (row (d); left column) in *piClim-control*. Differences with respect to *piClim-control* from *piClim-O3*, *piClim-NOx* and *piClim-VOC* can be seen in the second, third and right hand columns, respectively.**

While tropospheric column O_3 increases in both *piClim-NOx* and *piClim-VOC*, leading to positive contributions to the PD
705   tropospheric O_3 RF (Sect. 3.4.2), the global mean PD ERF is very different between the two simulations (+0.21 W m⁻² for *piClim-VOC* and -0.08 W m⁻² for *piClim-NOx* relative to *piClim-control*). Further, the spatial pattern of the ERF does not match those regions of largest O_3 changes. Instead, the dominant driver of the ERF differences is changes to OH and the subsequent impacts on aerosol particle formation and clouds. In particular, the positive tropospheric O_3 forcing in *piClim-NOx* (+0.2 W m⁻²) appears to be outweighed by a negative aerosol forcing, largely from aerosol-cloud interactions (aci) driven by

710   changes in oxidants and aerosol nucleation; the contribution to the global mean ERF from aerosol-radiation interactions (ari) is only -0.02 W m^{-2}, despite the strong regional changes in aerosol optical depth (AOD; Fig. 11; top row). Similarly, the forcing in *piClim-VOC* due to ari is negligible (0.00 W m^{-2}). However, the forcing in *piClim-VOC* due to aci enhances the positive tropospheric O$_3$ forcing (+0.07 W m^{-2}), leading to a global mean ERF of +0.21 ± 0.04 W m^{-2}.

715   A negative PD forcing attributable to NOx emissions has been found in other studies (Shindell et al., 2009; Collins et al., 2010) from a balance between the direct O$_3$ response (positive RF), the NOx-driven CH$_4$ response (negative RF), and the subsequent O$_3$ response to CH$_4$ changes (negative RF). Inclusion of ari and aci from sulphate and nitrate aerosol further increases the magnitude of the net negative forcing or cooling (Shindell et al., 2009; Collins et al., 2010). However, a study by Fry et al. (2012) found that the chemistry response is sensitive to the location of the emissions, with so large an uncertainty that it is

720   difficult to determine whether NOx emissions cause a warming or cooling. Indeed, other indirect effects such as NOx deposition to the terrestrial biosphere leading to fertilisation (Collins et al., 2010) and/or NOx-driven O$_3$ damage (Sitch et al., 2007; Collins et al., 2010) increase the uncertainty further through changes in carbon dioxide (CO$_2$). Thornhill et al. (2019) also shows that the ERF from PI-to-PD changes in NOx emissions among the AerChemMIP models differ in both sign and magnitude. Here, the longer time-scale CH$_4$ response to NOx emissions (Collins et al., 2010) is constrained, nitrate aerosol is

725   neglected (Sellar et al., 2019; Mulcahy et al., 2019), and CO$_2$ is concentration-driven (Sellar et al., 2019). Nevertheless, in UKESM1, the negative forcing due to aci from sulphate aerosol outweighs the positive NOx-driven O$_3$ RF, leading to a net negative ERF.

    Previous work has also found a positive PD SARF or RF from VOC and CO emissions, due to the combined indirect forcings by O$_3$ and CH$_4$ (Shindell et al., 2005; Forster et al., 2007); they estimate a global mean RF of +0.21 ± 0.10 W m^{-2} at the PD

730   (Year 1998) relative to PI (Year 1750). As was the case with NOx, the magnitude of this RF increases (to +0.25 ± 0.04 W m^{-2} for the year 2000) when additional indirect forcings from sulphate, nitrate, and CO$_2$ are included (Shindell et al., 2009). More recently, Stevenson et al. (2013) found the RF from VOC/CO emissions to be marginally higher, at +0.29 W m^{-2}, excluding aerosols, with contributions of 0.09, 0.08, and 0.12 W m^{-2} from O$_3$, CH$_4$, and CO$_2$, respectively. The RF contribution from O$_3$

735   alone quantified here (88 mW m^{-2}; Table 5) is consistent with the Stevenson et al. (2013) estimate. Despite excluding the longer-term CH$_4$ response and CO$_2$, the total global mean ERF from VOC/CO emissions of +0.21 ± 0.04 W m^{-2} is consistent with previous estimates of RF due to the additional positive contribution from aci driven by OH changes. However, Fry et al. (2014) found that the RF from VOCs is sensitive to the location of emissions and could influence the strength of the contribution from aerosols. Interestingly, other AerChemMIP models show a negative ERF from VOC and CO emissions

740   (Thornhill et al., 2019); these differences in sign of the ERF warrant further investigation.

    Despite the very different chemical response between NOx and VOC emissions, both in terms of the magnitude of the O$_3$ changes and the different impacts on OH, aerosols and clouds, a comparison of the global ERF changes (Table 3) indicates

that the PD ERF from *piClim-O3* is a linear combination of that from *piClim-NOx* and *piClim-VOC* for the NET, clear-sky

745 (CS) and the cloud radiative effect (CRE) components. Nevertheless, the results clearly suggest that Earth System (ES) interactions, particularly chemistry-aerosol coupling, can strongly affect estimates of climate forcing. Here, these interactions alter the PD ERF from tropospheric O_3 precursor emissions, while other studies (e.g. Shindell et al., 2009; Karset et al., 2018) show that they also affect estimates of PD anthropogenic aerosol forcing.

4.5 Other Forcings

750 **4.5.1 Near-Term Climate Forcers (NTCFs)**

The PD anthropogenic ERF due to CH_4, aerosols and O_3 abundances (also known as near-term climate forcers, NTCFs) was identified as the main source of uncertainty in the total anthropogenic ERF since pre-industrial times (Myhre et al., 2013a). This is due to the interaction between individual forcings, as well as the non-linear response of climate feedbacks due to aerosol-cloud interactions (Feichter et al., 2004; Deng et al., 2016; Collins et al., 2017). In this section, three experiments

755 related to NTCFs are discussed: the combined simulation (*piClim-NTCF*) is identical to *piClim-control* except that the aerosol and tropospheric O_3 precursor emissions (excluding CH_4) are set to PD (Year 2014) levels. The single-forcing runs change aerosol and aerosol precursor emissions only (*piClim-aer*), and tropospheric O_3 precursor emissions only (*piClim-O3*) from PI to PD levels. More details are described in Table 1.

760 The global mean ERF of NTCFs (excluding CH_4) at the PD relative to the PI is -1.12 ± 0.03 W m^{-2} (Table 3), where the 0.03 W m^{-2} is the standard error (Forster et al., 2016). The negative ERF results from the combination of a weak negative forcing in CS conditions (-0.04 ± 0.03 W m^{-2}) and a strong forcing due to the CRE (-1.08 ± 0.02 W m^{-2}). The weak negative forcing in the CS (NETcs) is due to the negative CS SW forcing (-0.29 ± 0.02 W m^{-2}) being largely offset by the CS LW forcing ($+0.24 \pm 0.02$ W m^{-2}). The negative CS SW forcing is closely correlated with changes in AOD (Figs. 12a, 12b). The CS LW component

765 of the ERF (LWcs) is positive ($+0.24 \pm 0.02$ W m^{-2}) due to both aerosols and O_3. The spatial variations in the global distribution of the LWcs component are closely related to land surface temperature (Ts) changes (Figs. 12c, 12d); the correlation coefficient is -0.81 with a statistical significance well over 99 %. Considering this good correlation, the increased LWcs may be in response to the Ts change due to NTCFs. The negative SWcre (-1.02 ± 0.03 W m^{-2}) is largely correlated with changes in cloudiness, with the spatial pattern correlation of -0.59 between the SWcre and total cloud fraction (Figs. 12e, 12f). The LW CRE (-0.06

770 ± 0.02 W m^{-2}) is the smallest in magnitude, with good correlation with the changes in high level cloud fraction (Figs. 12g, 12h). This is because the impact of cloud in the SW primarily depends on the cloud optical thickness, but the impact in the LW depends on the optically thin cloud for which both the optical depth and the cloud top temperature matter.
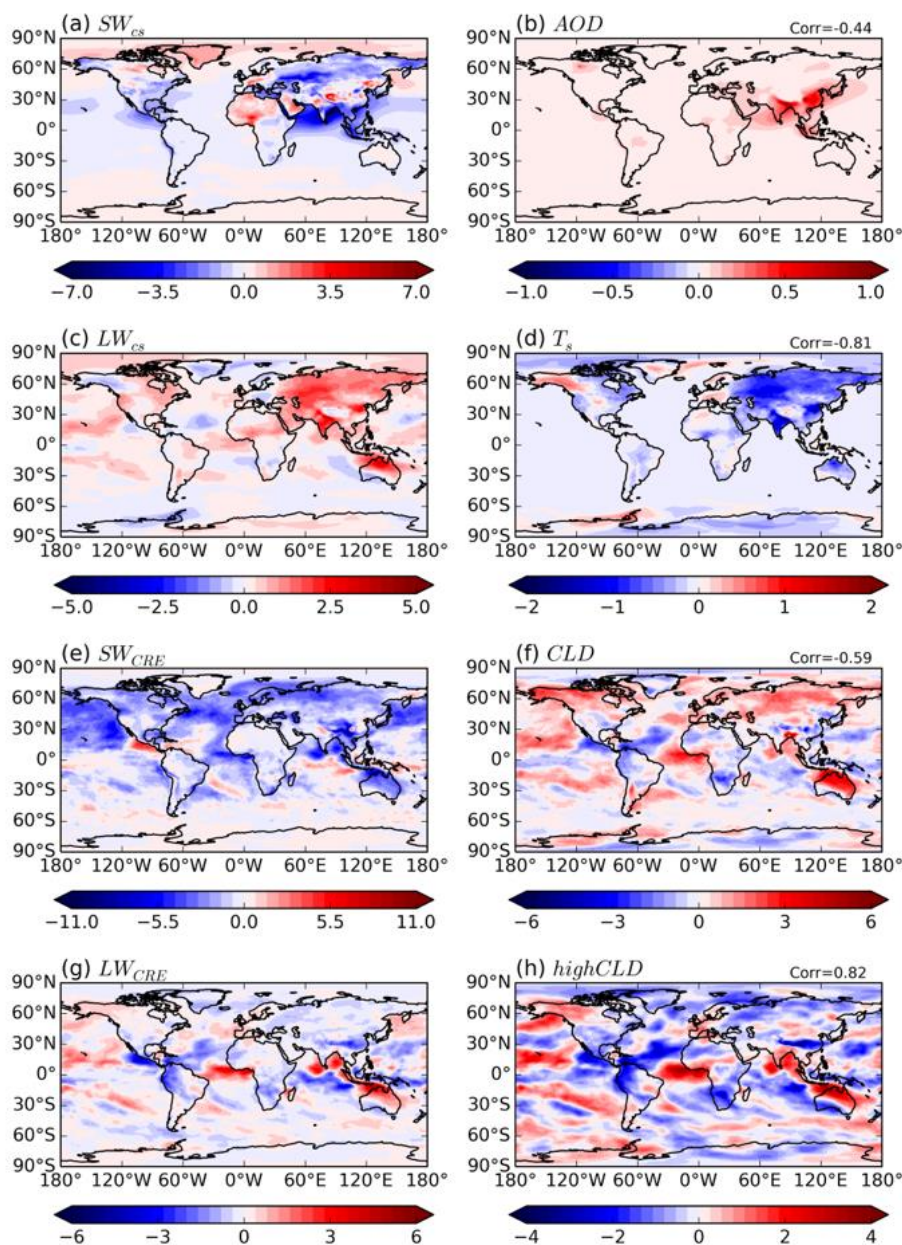
775

Figure 12: Spatial distribution of PD ERF relative to PI in W m⁻² derived from calculating the mean difference in the TOA radiative fluxes, (a) SWcs, (c) LWcs, (e) SWcre, (g) LWcre, and the changes (PD-PI) in (b) AOD at 550 nm, (d) surface temperature, (f) total cloud fraction, (h) high-level cloud fraction. The spatial pattern correlation between the left and right panel is shown in the right corner.

780

This study also attempts to estimate the effects of the non-linear interactions between the aerosol and O_3 forcings. When combined (aerosol and O_3), their interaction may induce an effect that differs from the sum of the individual single forcings. The ERFs do not add linearly, particularly in the net CS components (Table 3). Firstly, we calculate the aerosol IRFs. In

785   *piClim-NTCF,* it is -0.25 W m^{-2}, which is more negative than the sum of the aerosol IRF in *piClim-aer* (-0.16 W m^{-2}) and *piClim-O3* (-0.02 W m^{-2}). Secondly, the non-linearity may also be due to O_3. Photochemistry in the atmosphere is a well-known source of tropospheric O_3 and is determined by ambient level of tropospheric O_3 precursors (i.e. NOx and VOC/CO), and photolysis rates, which are largely influenced by meteorological factors such as solar irradiance and temperature (Xing et al., 2017). Despite no direct coupling between aerosols and photolysis in UKESM1 (Archibald et al., 2019), aerosol-mediated

790   cloud feedbacks result in SW reduction and surface cooling (Figs. 12a, 12d, 12e), which impact thermal and photochemical reactions leading to reduced photolysis rates in the lower troposphere, while enhancing the photolysis rate of O_3 in the upper troposphere (Figure 13). This is consistent with the vertical distribution of O_3 (not shown) and changes in surface O_3 (Fig. 14).
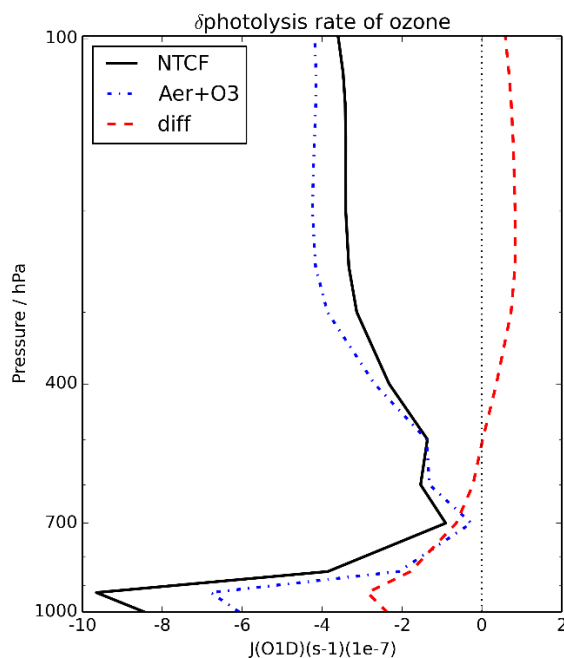
795   **Figure 13: Multi-annual global mean vertical distribution of changes (PD-PI) in j(O^{1}D) photolysis rate (10^{-7} s^{-1}). The black line indicates the effect of NTCFs in *piClim-NTCF* and the blue line indicates the effect of the sum of (*piclim-aer* + *piclim-O3*) relative to *piClim-control*. The red line indicates the difference between them.**
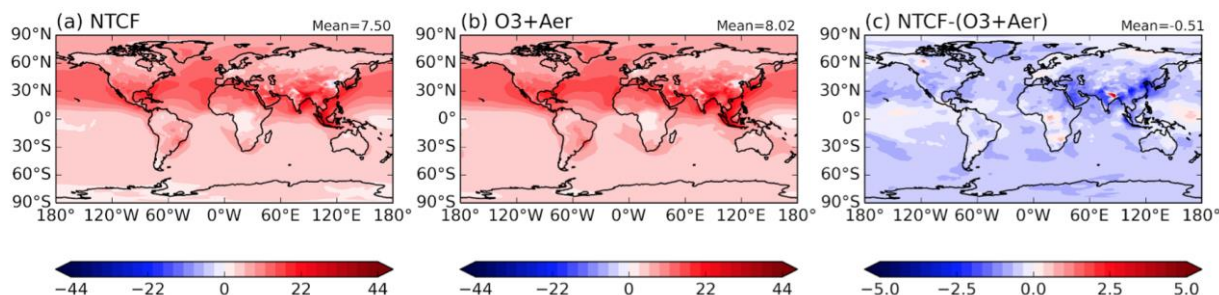
Figure 14: Spatial distribution of the PI-to-PD change in surface O3 volume mixing ratio (ppbv]) in (a) *piClim-NTCF* (b) the sum (*piClim-Aer* + *piClim-O3*) relative to *piClim-control*, (c) nonlinear interaction effects [*piClim-NTCF* − (*piClim-Aer* + *piClim-O3*)] between the aerosol and ozone forcing. The global average is shown in the right corner.

4.5.2 Land Use

Land-use change causes radiative forcing primarily by changing surface albedo; croplands and pastures have higher albedos than forests and are less able to mask the high albedo of snow cover. In UKESM1, historical land-use change causes surface cooling and this reduces outgoing LW radiation which acts to damp the negative SW ERF, reducing the magnitude of the ERF from -0.39 to -0.32 Wm^{-2}. The land-use ERF of UKESM1 is more negative than other estimates and outside the 'very likely' range (−0.25 to -0.05 Wm^{-2}) of AR5 (Andrews et al., 2017; Myhre et al., 2013a). However, its magnitude is reduced relative to UKESM1's predecessor, HadGEM2-ES (Collins et al., 2011), which produced a land-use ERF of -0.40 W m^{-2} (Andrews et al., 2017). Robertson (2019) showed that, even in the absence of snow cover, HadGEM2-ES had too strong an albedo response to land-use change and it is likely that this bias still exists in UKESM1.
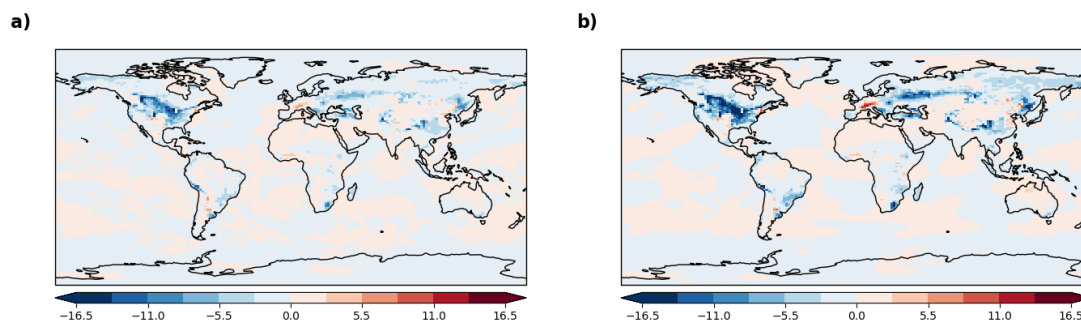
Figure 15: Global distribution of a) the total land-use ERF and b) the cloud-free and aerosol-free land-use ERF at the present day (Year 2014) relative to the pre-industrial (Year 1850) in W m^{-2}.

While the global mean land-use ERF is small, regionally it can be the dominant source of radiative forcing. Figure 15 shows the time-mean distribution of the land-use ERF and its cloud-free, aerosol-free, component which emphasizes the surface flux

contribution. The ERF is mostly constrained to regions of land-use change, with deforestation in North America and western Eurasia causing a negative ERF and increased tree cover in central Europe causing a positive ERF. Alongside the distribution

820 of land-use change itself, the magnitude of the ERF is larger in the mid-latitudes than the tropics, because the masking of snow cover by trees greatly increases the albedo response to changes in tree cover. The seasonality of leafiness, snow cover and insolation cause the land-use ERF to be largest in northern hemisphere summer (June to August mean of -0.53 W m^{-2}) and smallest in autumn (September to November mean of -0.16 W m^{-2}).

825 The land-use ERF is calculated by modifying three land-surface fields: land-cover, leaf area index (LAI) and canopy height. The values of the modified fields are taken from a coupled UKESM1 simulation that is forced only by historical land-use change. In the coupled configuration of UKESM1 (Sellar et al., 2019), the three land surface fields are prognostic fields calculated using a dynamic global vegetation model (DGVM), while in the atmosphere-only ERF configuration they are prescribed fields. This choice was made because the land-surface fields can be very slow to respond to changes in land-use

830 forcing and radiative forcing. In the coupled simulation of historical climate change including all forcings (*hist*), the land surface fields respond to changes in CO_2, climate and land-use, but if we use the land surface fields from this simulation, we find no substantial change in the land-use ERF (-0.35 W m^{-2}).

In addition to the radiative forcing caused by albedo changes, land-use change can alter climate via a number of other

835 mechanisms. Land-use change alters the land carbon sink. In particular, deforestation emits CO_2 to the atmosphere, and so some fraction of the CO_2 ERF is attributable to land-use change. Land-use change also affects surface climate via changes in roughness length and transpiration. These non-radiative mechanisms usually drive larger temperature changes than the albedo response and both the non-radiative mechanisms and the CO_2 forcings tend to oppose the albedo response.

4.5.3 Total Anthropogenic ERF

840 As summarized above, historical climate change has been driven by a wide range of anthropogenic forcings that act together, alongside natural forcings, to perturb the Earth's radiation balance. The total anthropogenic ERF is, therefore, a key metric in understanding observed and modelled changes in the climate system since the PI era. These various anthropogenic forcing mechanisms are not necessarily independent of each other and it is therefore worthwhile calculating the total anthropogenic ERF from a separate timeslice simulation including all forcings together (*piClim-anthro*; Pincus et al., 2016). We completed

845 a dedicated timeslice simulation with all anthropogenic forcings set to 2014 levels, including all GHGs (CO_2, N_2O, CH_4, HCs – both ODSs and non-ODSs), tropospheric O_3 precursors (VOC/CO and NOx), land-use changes, and anthropogenic aerosol or aerosol precursor emissions (SO_2, OC, BC). This experiment was not proposed in AerChemMIP (Collins et al., 2017) but is included here as part of RFMIP (Pincus et al., 2016). The main difference is that atmospheric chemistry in UKESM1 is fully interactive whereas other models participating in RFMIP (e.g. Andrews et al., 2019) use the CMIP6 ozone dataset to represent

850 changes in tropospheric and stratospheric O_3.

The UKESM1 *piClim-anthro* experiment leads to an ERF of 1.61 W m^{-2} (Table 3), which is dominated by a positive CS LW forcing due to GHGs and partially offset by a negative SW component due to aerosols and negative adjustments to LW and SW cloud-radiative effects (Table 3). This ERF is a little lower than the equivalent estimate from HadGEM3-GA7.1, which was 1.81 W m^{-2} (Andrews et al., 2019). The UKESM1 estimate is also somewhat lower than the median estimate from CMIP5 models assessed in AR5, which equates to approximately 1.9 W m^{-2} after adjustment to the reference period of 1861-1880 to 2010-11 (Andrews and Forster, 2019; hereafter AF19). AR5 also provided an overall central estimate of 2.2 W m^{-2} and a 5-95 % confidence range of 1.0 - 3.2 W m^{-2} (after adjustment to the same reference period as above in AF19) taking into account multiple streams of evidence. AF19 re-evaluated this as 2.3 W m^{-2} with a narrower range of 1.7 - 3.0 [5 - 95 % confidence] using a combination of atmospheric model outputs and observational constraints. The lower bound of this range was reduced to 1.5 W m^{-2} if larger uncertainties were assumed for the climate feedback parameter or for the global-mean surface temperatures anomalies used to constrain the forcing. The UKESM1 estimate of 1.61 W m^{-2} is therefore within the original uncertainty range given by AR5 but on the edge of the range proposed in AF19.

There are several factors that contribute to the relatively low estimate of anthropogenic ERF in UKESM1. Firstly, the anthropogenic aerosol forcing in UKESM1 (and GC3.1) is -1.13 W m^{-2} (well within the uncertainty range) and offsets a major portion of the positive GHG forcing (2.89 W m^{-2}). Secondly, the ERF from *piClim-HC* is negative (-0.33 W m^{-2}) due to a strong O$_3$ response and connected aerosol-mediated cloud feedbacks (Morgenstern et al., 2019). Thirdly, adjustments in vegetation lead to an appreciable negative ERF from land-use changes (-0.32 W m^{-2}). The stronger negative forcing from *piClim-HC* and *piClim-LU* largely explain why the UKESM1 estimate is ~0.2 W m^{-2} lower than HadGEM3-GA7.1. As shown in Fig. 3e, the negative contributions more than offset the positive GHG forcing in certain regions. For instance, the anthropogenic ERF is negative over large parts of North America and Asia (from a combination of land use change and aerosol forcing; see Figs. 3d and 3b), over the North Pacific (due to aerosol-cloud forcing) and at southern high latitudes (from O$_3$ depletion due to HCs, see Fig. 3a). In contrast, the anthropogenic forcing is strongly positive over the tropics and southern hemisphere sub-tropics (Fig. 3e) where the direct radiative effect of GHGs dominates.

The couplings between chemistry, aerosol and land surface processes included in UKESM1 increase the possibilities for non-linear feedbacks and interactions among the various anthropogenic forcing agents. However, these apparently have little net overall effect on the total forcing (1.61 W m^{-2}), which is almost identical to the sum of the forcings (1.59 W m^{-2}) from the four separate groups that it includes (GHG, aerosol, tropospheric O$_3$ precursors, and land use). The two estimates are not statistically different given the standard error on these is around 0.03 - 0.04 W m^{-2} (Table 3). This does not imply that the forcings act independently as it is possible that competing non-linear interactions cancel in this particular case. As shown in Sect. 4.5.1, the aerosol and tropospheric O$_3$ forcings did not add linearly, and neither did the sum of individual GHGs forcings (Sect. 4.2.4).

5 Conclusions

Quantifying forcings from anthropogenic perturbations to the Earth System (ES) is important for understanding changes in climate since the pre-industrial (PI) period. In this paper, we have quantified and analysed a wide range of PD anthropogenic forcings with the UK's Earth System Model (ESM), UKESM1 (Sellar et al., 2019), using the concept of effective radiative forcing (ERF). ERFs have been shown to be a more useful metric for evaluating and comparing the relative roles of diverse forcing agents due to the relationship to global-mean temperature and other impacts that scale with it. In particular, by quantifying ERFs within a full ESM, this study addresses gaps in previous assessments in which rapid adjustments were neglected and enables the role of indirect forcings and various climate-chemistry-aerosol-cloud feedbacks to be quantified.

We find that carbon dioxide (CO_2) exerts a global mean ERF of 1.82 W m^{-2} at the present-day (PD), consistent with previous estimates, making it the single largest contributor to PD climate forcing. However, UKESM1 appears to have a more pronounced surface warming adjustment associated with the physiological forcing by CO_2 than its successor, HadGEM2-ES. The nitrous oxide (N_2O) PD ERF quantified here (0.13 W m^{-2}) is lower than previous estimates due to indirect effects from ozone (O_3) depletion, and fast cloud adjustments; a shift of circulation results in a redistribution of clouds with clouds structure moving poleward. A warming associated with an O_3 increase in the tropical upper troposphere/lower stratosphere (UTLS) region may result in a regional suppression of convection and a reduction of associated LW radiation coming from cloud top. The PI-to-PD change in methane (CH_4) concentration leads to a global mean ERF of +0.93 W m^{-2}, with the majority of the forcing in the clear-sky longwave component. Given the inclusion of interactive chemistry in UKESM1, the ERF is larger than other estimates of direct CH_4 forcing as a result of indirect effects. O'Connor et al. (2019) apportion the CH_4 ERF between direct and indirect contributions as well as considering an emission-based perspective.

The global annual mean ERF from the PI to PD change in O_3 depleting substances (ODSs) is -0.33 W m^{-2}. A quantitative and process-based understanding of what's driving the negative ERF, despite our understanding to date of the relative roles of ODSs and O_3 depletion in climate forcing, is presented in Morgenstern et al. (2019). Considering all greenhouse gases (GHGs) together, we quantify a global mean ERF of 2.89 W m^{-2}, less than the 3.09 W m^{-2} estimate from the physical model HadGEM3-GC31, due to indirect effects. There is also some evidence of non-linearity between the combined GHG ERF and the sum of the individual GHG ERFs, potentially due to interactive O_3 and aerosol-mediated cloud feedbacks, which may warrant further investigation.

The new GLOMAP-mode aerosol scheme in UKESM1 (Mulcahy et al., 2019) leads to an intermediate sized negative ERF (-1.13 W m^{-2}) due to strong aerosol-cloud interactions (aci), despite strong absorption by black carbon (BC) and relatively weak negative aerosol instantaneous radiative forcing (IRF) from aerosol-radiation interactions (ari). Internal mixing and chemical

interactions included in the new aerosol scheme mean that neither aerosol IRF nor aci are linear (sulphate, organic carbon (OC), BC interact with one another) making the total aerosol ERF less than the sum of the individual ERFs.

920   Examining tropospheric O_3 radiative forcing alone, results from UKESM1 suggest that the contribution from CH_4 dominates (45 %), with nitrogen oxides (NOx) and volatile organic compound (VOC)/carbon monoxide (CO) contributing 36 and 19 %, respectively. These emissions-based contributions are well within the spread of estimates from ACCMIP (Stevenson et al., 2013): CH_4 (44 ± 12 %), NOx (31 ± 9 %), and VOC/CO (25 ± 3 %) although there is disagreement with other studies. Changes in oxidants, driven by the PI-to-PD changes in tropospheric O_3 precursor emissions, lead to an indirect aerosol ERF from aci,

925   which either supplements or offsets the positive ERF from tropospheric O_3, leading to global mean ERFs of 0.21 and -0.08 W m^{-2} for VOC/CO and NOx emissions changes, respectively. However, there appears to be disagreement across the AerChemMIP models on the sign and/or magnitude of the tropospheric O_3 precursor ERFs and further analysis to understand what's driving these differences is required.

930   The aerosol and tropospheric O_3 precursors (near-term climate forcers, NTCFs) together exert a global mean ERF of -1.12 W m^{-2}, which is mainly due to changes in the cloud radiative effect (CRE). There is also evidence of non-linearity in the global mean ERF between the combined *piClim-NTCF* experiment and the sum of the individual *piClim-aer* and *piclim-O3* experiments; this is mainly evident in the CS and is driven by changes in aerosol optical depth (AOD) and O_3. Land use (LU) change since the PI has also exerted a negative forcing at the PD, estimated to be -0.32 W m^{-2} on a global mean basis. However,

935   this estimate is outside the likely range from previous estimates, and is most likely due to too strong an albedo response.

Historical climate change has been driven by a wide range of anthropogenic forcings that act together, alongside natural forcings, to perturb the Earth's radiation balance. As a result, the total anthropogenic ERF is a key metric in understanding observed and modelled changes in the climate system since the PI era. The estimate of the total anthropogenic ERF from

940   UKESM1 is 1.61 W m^{-2}, which is relatively low compared to previous assessments; this is mainly due to an intermediate negative aerosol ERF, a modest negative LU forcing and strong stratospheric O_3 depletion. Although it may be biased low, that combined with high climate sensitivity means that UKESM1 reproduces historical global mean warming over the 1850 – 2014 period (Sellar et al., 2019).

945   In addition to quantifying anthropogenic PD ERFs with a fully coupled ESM, this study and other studies (e.g. Morgenstern et al., 2019; O'Connor et al., 2019) show the importance of indirect forcings and climate-aerosol-chemical feedbacks, and quantified their role within the ERF framework. There are substantial feedbacks between GHGs, stratospheric and tropospheric O_3, and aerosols, some of which act non-linearly. These effects demonstrate the importance of including Earth System (ES) interactions when quantifying PD climate forcing. In particular, we consider that rapid adjustments included in the definition

950   of ERF should include chemical as well as physical adjustments, consistent with Ramaswamy et al. (2019). They concluded

in their recent assessment that although the radiative forcing concept is simple, it needs to increasingly account for the complex relevant processes in the Earth System.

Acknowledgements

The development of the UK's Earth System Model, UKESM1, was funded by the Met Office Hadley Centre Climate
955   Programme funded by BEIS and Defra (GA01101) and by the National Environmental Research Council (NERC) national capability grant for the UK Earth System Modelling project, grant number NE/N017951/1. MD, GAF, CH, BJ, JPM, FMO'C, ER, and AW were funded by the Met Office Hadley Centre Climate Programme funded by BEIS and Defra (GA01101). GF, FMO'C and JCT also acknowledge the EU Horizon 2020 Research Programme CRESCENDO project, grant agreement number 641816. OM and GZ were supported by the NZ Government's Strategic Science Investment Fund (SSIF) through the
960   NIWA programme CACV. JW acknowledges support by the Deep South National Science Challenge (DSNSC), funded by the New Zealand Ministry for Business, Innovation and Employment (MBIE). BK, JS and SS were supported by the Korea Meteorological Administration Research and Development Program "Development and Assessment of IPCC AR6 Climate Change Scenario", grant agreement number 1365003000.

965   The authors acknowledge the contribution of NeSI high-performance computing facilities to the results of this research. New Zealand's national facilities are provided by the New Zealand eScience Infrastructure (NeSI) and funded jointly by NeSI's collaborator institutions and through MBIE's Research Infrastructure programme. This work used Monsoon2, a collaborative High Performance Computing facility funded by the Met Office and the Natural Environment Research Council. This work also used the NEXCS High Performance Computing facility funded by the Natural Environment Research Council and
970   delivered by the Met Office. This work used JASMIN, the UK collaborative data analysis facility; the authors are grateful for the provision of these facilities.

The authors thank T. Andrews for constructive comments on the manuscript. Last but not least, the authors wish to acknowledge the huge effort from the UKESM1 core group in building and evaluating UKESM1 and making it available for
975   use in RFMIP and AerChemMIP.

Data Availability

Data from all the simulations which underpin this paper are in the process of being post-processed in readiness for uploading to the Earth System Grid Federation (ESGF). The authors endeavour to use the precise data citation for each piece of data
980   once all of it is citable.

Author Contributions

The model simulations were set up, reviewed, and/or ran by FMO'C, NLA, MD, GF, PG, CH, BTJ, BK, JK, JPM, ER, SS, ST, AW, JW, and GZ. Data processing and upload to the Earth System Grid Federation (ESGF) was carried out by MD, BK, RK, MR, SS, JCT, and JW. Analysis was carried out by FMO'C, PG, BTJ, JK, JPM, ER, JS, SS, JCT, AW, and GZ. The manuscript was prepared by FMO'C, PG, BTJ, JK, OM, ER, JS, SS, JCT, AW, and GZ, with additional contributions from all co-authors.

Completing Interests

The authors declare that they have no conflict of interest.

References

Albrecht, B. A.: Aerosols, Cloud Microphysics, and Fractional Cloudiness, *Science*, 245, 1227–1230, DOI: 10.1126/science.245.4923.1227, 1989.

Andrews, T., J. M. Gregory, M. J. Webb, and K. E. Taylor: Forcing, feedbacks and climate sensitivity in CMIP5 coupled atmosphere-ocean climate models, *Geophys. Res. Lett.*, 39, L09712, doi:10.1029/ 2012GL051607, 2012a.

Andrews, T., M. A. Ringer, M. Doutriaux-Boucher, M. J. Webb, and W. J. Collins: Sensitivity of an Earth system climate model to idealized radiative forcing, *Geophys. Res. Lett.*, *39*(10), 2012b.

Andrews, T.: Using an AGCM to Diagnose Historical Effective Radiative Forcing and Mechanisms of Recent Decadal Climate Change, *J. Climate*, DOI: 10.1175/JCLI-D-13-00336.1, 2014.

Andrews, T., R. A. Betts, B. B. B. Booth, C. D. Jones, and G. S. Jones: Effective radiative forcing from historical land use change. *Climate Dyn.*, 48, 3489, doi.org/10.1007/s00382-016-3280-7, 2017.

Andrews, T., M. B. Andrews, A. Bodas-Salcedo, G. S. Jones, T. Kulhbrodt, J. Manners, M. B. Menary, J. Ridley, M. A. Ringer, A. A. Sellar, C. A. Senior, and Y. Tang: Forcings, feedbacks and climate sensitivity in HadGEM3-GC3.1 and UKESM1, *J. Adv. Modeling Earth Sys.*, Submitted, 2019.

Andrews, T., and P. M. Forster: Energy budget constraints on historical radiative forcing, *Nature Climate Change*, Submitted, 2019.

Archibald, A. T., M. C. Cooke, S. R. Utembe, D. E. Shallcross, R. G. Derwent, and M. E. Jenkin: Impacts of mechanistic changes on HOx formation and recycling in the oxidation of isoprene, *Atmos. Chem. Phys.*, 10, 8097–8118, doi:10.5194/acp-10-8097-2010, 2010.

Archibald, A. T., O'Connor, F. M., N. L. Abraham, S. Archer-Nicholls, M. P. Chipperfield, M. Dalvi, G. A. Folberth, F. Dennison, S. S. Dhomse, P. T. Griffiths, C. Hardacre, A. J. Hewitt, R. Hill, C. E. Johnson, J. Keeble, M. O. Köhler, O. Morgenstern, J. P. Mulcahy, C. Ordóñez, R. J. Pope, S. Rumbold, M. R. Russo, N. Savage, A. Sellar, M. Stringer, S. Turnock, O. Wild, and G. Zeng: Description and evaluation of the UKCA stratosphere-troposphere chemistry scheme (StratTrop vn 1.0) implemented in UKESM1, *Geosci. Model Dev. Disc.*, doi.org/10.5194/gmd-2019-246, 2019.

Arfeuille, F., D. Weisenstein, H. Mack, E. Rozanov, T. Peter, and S. Brönnimann: Volcanic forcing for climate modeling: a new microphysics-based data set covering years 1600–present, *Clim. Past*, 10, 359–375, doi:10.5194/cp-10-359-2014, 2014.

Arneth, A., S. P. Harrison, S. Zaehle, K. Tsigaridis, S. Menon, P. J. Bartlein, J. Feichter, A. Korhola, M. Kulmala, D. O'Donnell, G. Schurgers, S. Sorvari, and T. Vesala: Terrestrial biogeochemical feedbacks in the climate system, *Nature Geoscience*, 3, 525-532, 2010.

Bellouin, N., J. Rae, A. Jones, C. Johnson, J. Haywood, and O. Boucher: Aerosol forcing in the Climate Model Intercomparison Project (CMIP5) simulations by HadGEM2-ES and the role of ammonium nitrate, *J. Geophys. Res.*, 116, D20206, doi:10.1029/2011JD016074, 2011.

Bellouin, N., J. Quaas, E. Gryspeerdt, S. Kinne, P. Stier, D. Watson-Parris, O.Boucher, K. S. Carslaw, M. Christensen, A.-L. Daniau, J.-L. Dufresne, G. Feingold, S. Fiedler, P. Forster, A. Gettelman, J. M. Haywood, F. Malavelle, U. Lohmann, T. Mauritsen, D. T. McCoy, G. Myhre, J. Mülmenstädt, D. Neubauer, A. Possner, M. Rugenstein, Y. Sato, M. Schulz, S. E. Schwartz, O. Sourdeval, T. Storelvmo, V. Toll, D. Winker, and B. Stevens: Bounding aerosol radiative forcing of climate change, *Rev. Geophys.*, doi.org/10.1029/2019RG000660, In press, 2019.

Bond, T. C., S. J. Doherty, D. W. Fahey, P. M. Forster, T. Berntsen, B. J. DeAngelo, M. G. Flanner, S. Ghan, B. Kärcher, D. Koch, S. Kinne, Y. Kondo, P. K. Quinn, M. C. Sarofim, M. G. Schultz, M. Schulz, C. Venkataraman, H. Zhang, S. Zhang, N. Bellouin, S. K. Guttikunda, P. K. Hopke, M. Z. Jacobson, J. W. Kaiser, Z. Klimont, U. Lohmann, J. P. Schwarz, D. Shindell, T. Storelvmo, S. G. Warren, and C. S. Zender: Bounding the Role of Black Carbon in the Climate System: A Scientific Assessment, *J. Geophys. Res.-Atmos.*, 118, 5380–5552, doi.org/10.1002/jgrd.50171, 2013.

Boucher, O., D. Randall, P. Artaxo, C. Bretherton, G. Feingold, P. Forster, V.-M. Kerminen, Y. Kondo, H. Liao, U. Lohmann, P. Rasch, S.K. Satheesh, S. Sherwood, B. Stevens and X.Y. Zhang: Clouds and Aerosols. In: Climate Change 2013: The Physical Science Basis. Contribution of Working Group I to the Fifth Assessment Report of the Intergovernmental Panel on Climate Change [Stocker, T.F., D. Qin, G.-K. Plattner, M. Tignor, S.K. Allen, J. Boschung, A. Nauels, Y. Xia, V. Bex and P.M. Midgley (eds.)]. Cambridge University Press, Cambridge, United Kingdom and New York, NY, USA, 2013.

Butchart, N.: The Brewer-Dobson circulation, *Rev. Geophys.*, 52, 157–184, doi:10.1002/2013RG000448, 2014.

Carslaw, K. S., L. A. Lee, C. L. Reddington, K. J. Pringle, A. Rap, P. M. Forster, G. W. Mann, D. V. Spracklen, M. T. Woodhouse, L. A. Regayre, and J. R. Pierce: Large contribution of natural aerosols to uncertainty in indirect forcing, *Nature*, 503, 67-71, DOI:10.1038/nature12674, 2013.

Checa-Garcia, R., Hegglin, M. I., Kinnison, D., Plummer, D. A., and K. P. Shine: Historical tropospheric and stratospheric ozone radiative forcing using the CMIP6 database, *Geophys. Res. Lett.*, 45, 3264–3273, doi.org/10.1002/2017GL076770, 2018.

Chung, E.-S., and B. J. Soden: An assessment of methods for computing radiative forcing in climate models, *Environ. Res. Lett.*, 10, 074004, 2015.

Collins, W. D., V. Ramaswamy, M. D. Schwarzkopf, Y. Sun, R. W. Portmann, Q. Fu, S. E. B. Casanova, J.-L. Dufresne, D. W. Fillmore, P. M. D. Forster, V. Y. Galin, L. K. Gohar, W. J. Ingram, D. P. Kratz, M.-P. Lefebvre, J. Li, P. Marquet, V. Oinas, Y. Tsushima, T. Uchiyama, and W. Y. Zhong: Radiative forcing by well-mixed greenhouse gases: Estimates from climate models in the Intergovernmental Panel on Climate Change (IPCC) Fourth Assessment Report (AR4), *J. Geophys. Res.*, 111, D14317, doi:10.1029/2005JD006713, 2006.

Collins, W. J., S. Sitch, and O. Boucher: How vegetation impacts affect climate metrics for ozone precursors, *J. Geophys. Res.*, 115, D23308, doi:10.1029/2010JD014187, 2010.

Collins, W. J., N. Bellouin, M. Doutriaux-Boucher, N. Gedney, P. Halloran, T. Hinton, J. Hughes, C. D. Jones, M. Joshi, S. Liddicoat, G. Martin, F. O'Connor, J. Rae, C. Senior, S. Sitch, I. Totterdell, A. Wiltshire, and S. Woodward: Development and evaluation of an Earth-System model – HadGEM2, *Geosci. Model Dev.*, 4, 1051–1075, doi:10.5194/gmd-4-1051-2011, 2011.

Collins, W. J., J.-F. Lamarque, M. Schulz, O. Boucher, V. Eyring, M. I. Hegglin, A. Maycock, G. Myhre, M. Prather, D. Shindell, and S. J. Smith: AerChemMIP: quantifying the effects of chemistry and aerosols in CMIP6, *Geosci. Model Dev.*, 10, 585-607, doi.org/10.5194/gmd-10-585-2017, 2017.

Deng, J., H. Xu, and L. Zhang: Nonlinear effects of anthropogenic aerosol and urban land surface forcing on spring climate in eastern China, *J. Geophys. Res.*, 121, 4581-4599, doi:10.1002/2015JD024377, 2016.

Doutriaux-Boucher, M., M. J. Webb, J. M. Gregory, and O. Boucher: Carbon dioxide induced stomatal closure increases radiative forcing via a rapid reduction in low cloud, *Geophys. Res. Lett.*, *36*(2), 2009.

Edwards, J. M. and A. Slingo: Studies with a flexible new radiation code. I: Choosing a configuration for a large-scale model, *Q. J. R. Meteorol. Soc.*, 122, pp. 689-719, 1996.

Engel, A. and M. Rigby (Lead Authors), J.B. Burkholder, R.P. Fernandez, L. Froidevaux, B.D. Hall, R. Hossaini, T. Saito, M.K. Vollmer, and B. Yao: Update on Ozone-Depleting Substances (ODSs) and Other Gases of Interest to the Montreal Protocol, Chapter 1 in Scientific Assessment of Ozone Depletion: 2018, Global Ozone Research and Monitoring Project–Report No. 58, World Meteorological Organization, Geneva, Switzerland, 2018.

Etminan, M., G. Myhre, E. J. Highwood, and K. P. Shine: Radiative forcing of carbon dioxide, methane, and nitrous oxide: A significant revision of the methane radiative forcing, *Geophys. Res. Lett.*, 43, 12614–12623, doi:10.1002/2016GL071930, 2016.

Eyring, V., S. Bony, G. A. Meehl, C. A. Senior, B. Stevens, R. J. Stouffer, and K. E. Taylor: Overview of the Coupled Model Intercomparison Project Phase 6 (CMIP6) experimental design and organization, *Geosci. Model Dev.*, 9, 1937-1958, doi.org/10.5194/gmd-9-1937-2016, 2016.

Feichter, J., E. Roeckner, U. Lohmann, and B. Liepert: Nonlinear aspects of the climate response to greenhouse gas and aerosol forcing, *J. Climate*, 17, 2384-2398, doi:10.1175/1520-0442(2004)017, 2004.

Feng, Y., V. Ramanathan, and V. R. Kotamarthi: Brown carbon: a significant atmospheric absorber of solar radiation?, *Atmos. Chem. Phys.*, 13, 8607–8621, doi.org/10.5194/acp-13-8607-2013, 2013.

Fiore, A. M., F. J. Dentener, O. Wild, C. Cuvelier, M. G. Schultz, P. Hess, C. Textor, M. Schulz, R. M. Doherty, L. W. Horowitz, I. A. MacKenzie, M. G. Sanderson, D. T. Shindell, D. S. Stevenson, S. Szopa, R. Van Dingenen, G. Zeng, C. Atherton, D. Bergmann, I. Bey, G. Carmichael, 1W. J. Collins, B. N. Duncan, G. Faluvegi, G. Folberth, M. Gauss, S. Gong, D. Hauglustaine, T. Holloway, I. S. A. Isaksen, D. J. Jacob, J. E. Jonson, J. W. Kaminski, T. J. Keating, A. Lupu, E. Marmer, V. Montanaro, R. J. Park, G. Pitari, K. J. Pringle, J. A. Pyle, S. Schroeder, M. G. Vivanco, P. Wind, G. Wojcik, S. Wu, and A. Zuber: Multimodel estimates of intercontinental source-receptor relationships for ozone pollution, *J. Geophys. Res.*, 114, D04301, doi:10.1029/2008JD010816, 2009.

Forster, P., V. Ramaswamy, P. Artaxo, T. Berntsen, R. Betts, D.W. Fahey, J. Haywood, J. Lean, D.C. Lowe, G. Myhre, J. Nganga, R. Prinn, G. Raga, M. Schulz and R. Van Dorland: Changes in Atmospheric Constituents and in Radiative Forcing. In: Climate Change 2007: The Physical Science Basis. Contribution of Working Group I to the Fourth Assessment Report of the Intergovernmental Panel on Climate Change [Solomon, S., D. Qin, M. Manning, Z. Chen, M. Marquis, K.B. Averyt, M.Tignor and H.L. Miller (eds.)]. Cambridge University Press, Cambridge, United Kingdom and New York, NY, USA, 2007.

Forster, P. M., T. Andrews, P. Good, J. M. Gregory, L. S. Jackson, and M. Zelinka: Evaluating adjusted forcing and model spread for historical and future scenarios in the CMIP5 generation of climate models, *J. Geophys. Res. Atmos.*, 118, 1139–1150, doi:10.1002/jgrd.50174, 2013.

Forster, P. M., T. Richardson, A. C. Maycock, C. J. Smith, B. H. Samset, G. Myhre, T. Andrews, R. Pincus, and M. Schulz: Recommendations for diagnosing effective radiative forcing from climate models for CMIP6, *J. Geophys. Res. Atmos.*,121,12460–12475, doi:10.1002/2016JD025320, 2016.

Fry, M. M., V. Naik, J. J. West, M. D. Schwarzkopf, A. M. Fiore, W. J. Collins, F. J. Dentener, D. T. Shindell, C. Atherton, D. Bergmann, B. N. Duncan, P. Hess, I. A. MacKenzie, E. Marmer, M. G. Schultz, S. Szopa, O. Wild, and G. Zeng: The influence of ozone precursor emissions from four world regions on tropospheric composition and radiative climate forcing, *J. Geophys. Res.*, 117, D07306, doi:10.1029/2011JD017134, 2012.

Fry, M. M., M. D. Schwarzkopf, Z. Adelman, and J. J. West: Air quality and radiative forcing impacts of anthropogenic volatile organic compound emissions from ten world regions, *Atmos. Chem. Phys.*, 14, 523–535, doi:10.5194/acp-14-523-2014, 2014.

Ghan, S.J., X. Liu, R.C. Easter, R. Zaveri, P.J. Rasch, J. Yoon, and B. Eaton: Toward a Minimal Representation of Aerosols in Climate Models: Comparative Decomposition of Aerosol Direct, Semidirect, and Indirect Radiative Forcing. *J. Climate,* 25, 6461–6476, https://doi.org/10.1175/JCLI-D-11-00650.1, 2012.

Ghan, S. J.: Technical Note: Estimating aerosol effects on cloud radiative forcing, *Atmos. Chem. Phys.*, 13, 9971-9974, https://doi.org/10.5194/acp-13-9971-2013, 2013.

Ghan, S., M. Wang, S. Zhang, S. Ferrachat, A. Gettelman, J. Griesfeller, Z. Kipling, U. Lohmann, H. Morrison, D. Neubauer, D. G. Partridge, P. Stier, T. Takemura, H. Wang, K. Zhang: Constraining aerosol effects on cloud forcing, P. Natl. Acad. Sci. USA, 113 (21) 5804-5811; DOI: 10.1073/pnas.1514036113, 2016.

Hansen, J., Sato, M., and R. Ruedy: Radiative Forcing and Climate Response, *J. Geophys. Res.*, 102, D6, 6831-6864, 1997.

Hansen, J., M. Sato, R. Ruedy, L. Nazarenko, A. Lacis, G. A. Schmidt, G. Russell, I. Aleinov, M. Bauer, S. Bauer, N. Bell, B. Cairns, V. Canuto, M. Chandler, Y. Cheng, A. Del Genio, G. Faluvegi, E. Fleming, A. Friend, T. Hall, C. Jackman, M. Kelley, N. Kiang, D. Koch, J. Lean, J. Lerner, K. Lo, S. Menon, R. Miller, P. Minnis, T. Novakov, V. Oinas, Ja. Perlwitz, Ju. Perlwitz, D. Rind, A. Romanou, D. Shindell, P. Stone, S. Sun, N. Tausnev, D. Thresher, B. Wielicki, T. Wong, M. Yao, and S. Zhang: Efficacy of climate forcings, J. Geophys. Res., 110, D18104, doi:10.1029/2005JD005776, 2005.

Hewitt, H. T., D. Copsey, I. D. Culverwell, C. M. Harris, R. S. R. Hill, A. B. Keen, A. J. McLaren, and E. C. Hunke: Design and implementation of the infrastructure of HadGEM3: the next-generation Met Office climate modelling system, *Geosci. Model Dev.*, 4, 223–253, doi: 10.5194/gmd-4-223-2011, 2011.

Hoesly, R. M., S. J. Smith, L. Feng, Z. Klimont, G. Janssens-Maenhout, T. Pitkanen, J. J. Seibert, L. Vu, R. J. Andres, R. M. Bolt, T. C. Bond, L. Dawidowski, N. Kholod, J. Kurokawa, M. Li, L. Liu, Z. Lu, M. C. P. Moura, P. R. O'Rourke, and Q. Zhang: Historical (1750–2014) anthropogenic emissions of reactive gases and aerosols from the Community Emissions Data System (CEDS), *Geosci. Model Dev.*, 11, 369-408, doi.org/10.5194/gmd-11-369-2018, 2018.

Holmes, C. D., M. J. Prather, O. A. Søvde, and G. Myhre: Future methane, hydroxyl, and their uncertainties: key climate and emission parameters for future predictions, *Atmos. Chem. Phys.*, 13, 285–302, doi.org/10.5194/acp-13-285-2013, 2013.

Johnson, B. T., J. M. Haywood, and M. K. Hawcroft: Are changes in atmospheric circulation important for black carbon aerosol impacts on clouds, precipitation, and radiation? *J. Geophys. Res.: Atmospheres*, 124, 7930– 7950, doi.org/10.1029/2019JD030568, 2019.

1175 Jones, A., Roberts, D. L., and A. Slingo: A climate model study of indirect radiative forcing by anthropogenic sulphate aerosols, *Nature*, 370, 450–453, https://www.nature.com/articles/370450a0, 1994.

Karset, I. H. H., T. K. Berntsen, T. Storelvmo, K. Alterskjæ , A. Grini , D. Olivié , A. Kirkevåg , Ø. Seland, T. Iversen, and M. Schulz: Strong impacts on aerosol indirect effects from historical oxidant changes, *Atmos. Chem. Phys.*, 18, 7669–7690,
1180 doi.org/10.5194/acp-18-7669-2018, 2018.

Kelly, J., R. M. Doherty, F. M. O'Connor, and G.W. Mann: The impact of biogenic, anthropogenic, and biomass burning emissions on regional and seasonal variations in secondary organic aerosol concentrations, *Atmos. Chem. Phys.*, doi.org/10.5194/acp-18-7393-2018, 2018.

1185
Lamarque, J.-F., D. T. Shindell, B. Josse, P. J. Young, I. Cionni, V. Eyring, D. Bergmann, P. Cameron-Smith, W. J. Collins, R. Doherty, S. Dalsoren, G. Faluvegi, G. Folberth, S. J. Ghan, L. W. Horowitz, Y. H. Lee, I. A. MacKenzie, T. Nagashima, V. Naik, D. Plummer, M. Righi, S. T. Rumbold, M. Schulz, R. B. Skeie, D. S. Stevenson, S. Strode, K. Sudo, S. Szopa, A. Voulgarakis, and G. Zeng: Atmospheric Chemistry and Climate Model Intercomparison Project (ACCMIP): overview and
1190 description of models, simulations and climate diagnostics, *Geosci. Model Dev.*, 6, 179–206, doi:10.5194/gmd-6-179-2013, 2013.

Li, J., C. L. Curry, Z. Sun, and F. Zhang: Overlap of solar and infrared spectra and the shortwave radiative effect of methane, *J. Atmos. Sci.*, 67(7), 2372–2389, doi:10.1175/2010jas3282.1, 2010.

1195
Lohmann, U., L. Rotstayn, T. Storelvmo, A. Jones, S. Menon, J. Quaas, A. M. L. Ekman, D. Koch, and R. Ruedy: Total aerosol effect: radiative forcing or radiative flux perturbation?, Atmos. Chem. Phys., 10, 3235–3246, www.atmos-chem-phys.net/10/3235/2010/, 2010.

1200 Malavelle, F., J. Haywood, A. Jones, A. Gettelman, L. Clarisse, S. Bauduin, R. P. Allan, I. H. H. Karset, J. Egill Kristjánsson, L. Oreopoulos, N. Cho, D. Lee, N. Bellouin, O. Boucher, D. P. Grosvenor, K. S. Carslaw, S. Dhomse, G. W. Mann, A. Schmidt, H. Coe, M. E. Hartley, M. Dalvi, A. A. Hill, B. T. Johnson, C. E. Johnson, J. R. Knight, F. M. O'Connor, D. G. Partridge, P. Stier, G. Myhre, S. Platnick, G. L. Stephens, H. Takahashi, and T. Thordarson: Strong constraints on aerosol–cloud interactions from volcanic eruptions, *Nature,* 546, 485–491, doi:10.1038/nature22974, 2017.

1205
Mann, G. W., K. S. Carslaw, D. V. Spracklen, D. A. Ridley, P. T. Manktelow, M. P. Chipperfield, S. J. Pickering, and C. E. Johnson: Description and evaluation of GLOMAP-mode: a modal global aerosol microphysics model for the UKCA composition-climate model, *Geosci. Model Dev.*, 3, 519–551, doi:10.5194/gmd-3-519-2010, 2010.

1210 Matthes, K., B. Funke, M. E. Andersson, L. Barnard, J. Beer, P. Charbonneau, M. A. Clilverd, T. Dudok de Wit, M. Haberreiter, A. Hendry, C. H. Jackman, M. Kretzschmar, T. Kruschke, M. Kunze, U. Langematz, D. R. Marsh, A. C. Maycock, S. Misios, C. J. Rodger, A. A. Scaife, A. Seppälä, M. Shangguan, M. Sinnhuber, K. Tourpali, I. Usoskin, M. van de Kamp, P. T. Verronen, and S. Versick: Solar forcing for CMIP6 (v3.2), *Geosci. Model Dev.*, 10, 2247-2302, doi.org/10.5194/gmd-10-2247-2017, 2017.

1215
van Marle, M. J. E., S. Kloster, B. I. Magi, J. R. Marlon, A.-L. Daniau, R. D. Field, A. Arneth, M. Forrest, S. Hantson, N. M. Kehrwald, W. Knorr, G. Lasslop, F. Li, S. Mangeon, C. Yue, J. W. Kaiser, and G. R. van der Werf: Historic global biomass burning emissions for CMIP6 (BB4CMIP) based on merging satellite observations with proxies and fire models (1750–2015), *Geosci. Model Dev.*, 10, 3329-3357, doi.org/10.5194/gmd-10-3329-2017, 2017.

1220

Meinshausen, M., E. Vogel, A. Nauels, K. Lorbacher, N. Meinshausen, D. M. Etheridge, P. J. Fraser, S. A. Montzka, P. J. Rayner, C. M. Trudinger, P. B. Krummel, U. Beyerle, J. G. Canadell, J. S. Daniel, I. G. Enting, R. M. Law, C. R. Lunder, S. O'Doherty, R. G. Prinn, S. Reimann, M. Rubino, G. J. M. Velders, M. K. Vollmer, R. H. J. Wang, and R. Weiss: Historical greenhouse gas concentrations for climate modelling (CMIP6), *Geosci. Model Dev.*, 10, 2057-2116, doi.org/10.5194/gmd-10-2057-2017, 2017.

Morgenstern, O., P. Braesicke, F. M. O'Connor, A. C. Bushell, C. E. Johnson, S. M. Osprey, and J. A. Pyle: Evaluation of the new UKCA climate-composition model – Part 1: The stratosphere, *Geosci. Model Dev.*, 2, 43-57, doi.org/10.5194/gmd-2-43-2009, 2009.

Morgenstern, O., F. M. O'Connor, B. Johnson, G. Zeng, J. P. Mulcahy, J. Williams, and J. Teixeira, M. Michou, P. Nabat, L. Horowitz, V. Naik, and L. Sentman: Reappraisal of the climate impacts of ozone-depleting substances, In preparation, 2019.

Mulcahy, J. P., Jones, C., Sellar, A., Johnson, B., Boutle, I. A., Jones, A., T. Andrews, S. T. Rumbold, J. Mollard, N. Bellouin, C. E. Johnson, K. D. Williams, D. P. Grosvenor, and D. T. McCoy: Improved aerosol processes and effective radiative forcing in HadGEM3 and UKESM1, *J. Adv. Modeling Earth Sys.*, 10, 2786–2805, doi.org/10.1029/2018MS001464, 2018.

Mulcahy, J. P., Johnson C., Jones C., Povey A., Sellar A., Scott C. E., Turnock S. T., Woodhouse M. T., Abraham L. N., Andrews M., Bellouin N., Browse J., Carslaw K. S., Dalvi M., Folberth G., Grosvenor D., Hardacre C., Johnson B., Jones A., Kipling Z., Mann G., Mollard J., Schutgens N., O'Connor F., Palmieri J., Reddington C., Richardson M., Stier P., Woodward S., and Yool A.: Description and evaluation of aerosol in UKESM1 and HadGEM3-GC3.1 CMIP6 historical simulations, *Geosci. Model. Dev.,* Submitted, 2019.

Myhre, G., E. Highwood, K. Shine, and F. Stordal: New estimates of radiative forcing due to well mixed greenhouse gases, *Geophys. Res. Lett.*, 25(14), 2715–2718, doi:10.1029/98GL01908, 1998.

Myhre, G., D. Shindell, F.-M. Bréon, W. Collins, J. Fuglestvedt, J. Huang, D. Koch, J.-F. Lamarque, D. Lee, B. Mendoza, T. Nakajima, A. Robock, G. Stephens, T. Takemura and H. Zhang (2013a): Anthropogenic and Natural Radiative Forcing. In: Climate Change 2013: The Physical Science Basis. Contribution of Working Group I to the Fifth Assessment Report of the Intergovernmental Panel on Climate Change [Stocker, T.F., D. Qin, G.-K. Plattner, M. Tignor, S.K. Allen, J. Boschung, A. Nauels, Y. Xia, V. Bex and P.M. Midgley (eds.)]. Cambridge University Press, Cambridge, United Kingdom and New York, NY, USA.

Myhre, G., Samset, B. H., Schulz, M., Balkanski, Y., Bauer, S., Berntsen, T. K., Bian, H., Bellouin, N., Chin, M., Diehl, T., Easter, R. C., Feichter, J., Ghan, S. J., Hauglustaine, D., Iversen, T., Kinne, S., Kirkevåg, A., Lamarque, J.-F., Lin, G., Liu, X., Lund, M. T., Luo, G., Ma, X., van Noije, T., Penner, J. E., Rasch, P. J., Ruiz, A., Seland, Ø., Skeie, R. B., Stier, P., Takemura, T., Tsigaridis, K., Wang, P., Wang, Z., Xu, L., Yu, H., Yu, F., Yoon, J.-H., Zhang, K., Zhang, H., and Zhou, C. (2013b): Radiative forcing of the direct aerosol effect from AeroCom Phase II simulations, *Atmos. Chem. Phys.*, 13, 1853-1877, doi.org/10.5194/acp-13-1853-2013.

Nisbet, E. G., E. J. Dlugokencky, M. R. Manning, D. Lowry, R. E. Fisher, J. L. France, S. E. Michel, J. B. Miller, J. W. C. White, B. Vaughn, P. Bousquet, J. A. Pyle, N. J. Warwick, M. Cain, R. Brownlow, G. Zazzeri, M. Lanoisellé, A. C. Manning, E. Gloor, D. E. J. Worthy, E.-G. Brunke, C. Labuschagne, E. W. Wolff, and A. L. Ganesan (2016): Rising atmospheric methane: 2007–2014 growth and isotopic shift, *Global Biogeochem. Cycles*, 30, 1356–1370, doi:10.1002/2016GB005406.

O'Connor, F. M., O. Boucher, N. Gedney, C.D. Jones, G.A. Folberth, R. Coppell, P. Friedlingstein, W.J. Collins, J. Chappellaz, J. Ridley, and C.E. Johnson (2010): The possible role of wetlands, permafrost and methane hydrates in the future methane cycle: A review, *Rev. Geophys.*, 48, RG4005, doi:10.1029/2010RG000326.

O'Connor, F. M., C. E. Johnson, O. Morgenstern, N. L. Abraham, P. Braesicke, M. Dalvi, G. A. Folberth, M. G. Sanderson,

P. J. Telford, A. Voulgarakis, P. J. Young, G. Zeng, W. J. Collins, and J. A. Pyle (2014): Evaluation of the new UKCA climate-composition model. Part II. The troposphere, *Geosci. Model Dev.*, 7, 41-91, doi.org/10.5194/gmd-7-41-2014.

O'Connor, F. M., O. Jamil, T. Andrews, B. T. Johnson, J. P. Mulcahy, and J. Manners (2019): Apportionment of the Pre-Industrial to Present-Day Climate Forcing by Methane using UKESM1, J. Adv. Modeling Earth Sys., Submitted.

Parrish, D. D., J.-F. Lamarque, V. Naik, L. Horowitz, D. T. Shindell, J. Staehelin, R. Derwent, O. R. Cooper, H. Tanimoto, A. Volz-Thomas, S. Gilge, H.-E. Scheel, M. Steinbacher, and M. Fröhlich (2014): Long-term changes in lower tropospheric baseline ozone concentrations: Comparing chemistry-climate models and observations at northern midlatitudes, *J. Geophys. Res. Atmos.*, 119, 5719–5736, doi:10.1002/ 2013JD021435.

Pincus, R., P. M. Forster, and B. Stevens (2016): The Radiative Forcing Model Intercomparison Project (RFMIP): experimental protocol for CMIP6, *Geosci. Model Dev.*, 9, 3447–3460, www.geosci-model-dev.net/9/3447/2016/.

Prather, M. J. (1996): Time scales in atmospheric chemistry: Theory, GWPs for CH4 and CO, and runaway growth, *Geophys. Res. Lett.*, 23, 2597–2600, doi:10.1029/96GL02371.

Prather, M. J., Ehhalt, D., Dentener, F., Derwent, R., Dlugokencky, E., Holland, E., Isaksen, I., Katima, J., Kirchoff, V., Matson, P., Midgley, P. and Wang, M.: Atmospheric chemistry and greenhouse gases, in: Climate Change 2001: The Scientific Basis. Contribution of Working Group I to the Third Assessment Report of the Intergovernmental Panel on Climate Change, Houghton, J. T., Ding, Y., Griggs, D. J., Noguer, M., van der Linden, P. J., Dai, X., Maskell, K., and Johnson, C. A., Cambridge University Press, Cambridge, UK, 329–287, 2001.

Prather, M. J., and J. Hsu (2010): Coupling of Nitrous Oxide and Methane by Global Atmospheric Chemistry
Science, Vol. 330, 6006, 952-954, DOI: 10.1126/science.1196285.

Ramaswamy, V., O. Boucher, J. Haigh, D. Hauglustaine, J. Haywood, G. Myhre, T. Nakajima, G. Y. Shi, and S. Solomon (2001), Radiative forcing of climate change, in Climate Change 2001: The Scientific Basis. Contribution of Working Group I to the Third Assessment Report of the Intergovernmental Panel on Climate Change, edited by Y. Ding et al., Cambridge Univ. Press, Cambridge and New York.

Ramaswamy, V., W. Collins, J. Haywood, J. Lean, N. Mahowald, G. Myhre, V. Naik, K.P. Shine, B. Soden, G. Stenchikov, and T. Storelvmo (2019): Radiative Forcing of Climate: The Historical Evolution of the Radiative Forcing Concept, the Forcing Agents and their Quantification, and Applications, Accepted, American Meteorol. Soc. Centenary Monograph, DOI 10.1175/AMSMONOGRAPHS-D-19-0001.1 .

Rap, A., N. A. D. Richards, P. M. Forster, S. A. Monks, S. R. Arnold, and M. P. Chipperfield (2015): Satellite constraint on the tropospheric ozone radiative effect, *Geophys. Res. Lett.*, 42, 5074–5081, doi:10.1002/2015GL064037.

Richardson, T.B., Forster, P.M., Andrews, T., Boucher, O., Faluvegi, G., Fläschner, D., Kasoar, M., Kirkevåg, A., Lamarque, J.F., Myhre, G. and Olivié, D. (2018): Carbon dioxide physiological forcing dominates projected eastern Amazonian drying. *Geophys. Res. Lett.*, *45*(6), pp.2815-2825.

Robertson, E. (2019): The Local Biophysical Response to Land-Use Change in HadGEM2-ES, *J. Climate,* 32, 7611–7627, doi.org/10.1175/JCLI-D-18-0738.1.

Saleh, R., et al. (2014), Brownness of organics in aerosols from biomass burning linked to their black carbon content, *Nat. Geosci.*, doi:10.1038/NGEO2220.

Sellar, A. A., C. G. Jones,, J. Mulcahy, Y. Tang, A. Yool, A. Wiltshire, F. M. O'Connor, M. Stringer, R. Hill, J. Palmieri, S. Woodward, L. de Mora, T. Kuhlbrodt, S. Rumbold, D. I. Kelley, R. Ellis, C. E. Johnson, J. Walton, N. L. Abraham, M. B. Andrews, T. Andrews, A. T. Archibald, S. Berthou, E. Burke, E. Blockley, K. Carslaw, M. Dalvi, J. Edwards, G. A. Folberth, N. Gedney, P. T. Griffiths, A. B. Harper, M. A. Hendry, A. J. Hewitt, B. Johnson, A. Jones, C. D. Jones, J. Keeble, S. Liddicoat, O. Morgenstern, R. J. Parker, V. Predoi, E. Robertson, A. Siahaan, R. S. Smith, R. Swaminathan, M. Woodhouse, G. Zeng, and M. Zerroukat (2019): UKESM1: Description and evaluation of the UK Earth System Model, *J. Adv. Modeling Earth Sys.*, doi.org/10.1029/2019MS001739, In press.

Sherwood, S., P. M. Forster, J. Gregory, S. Bony, B. Stevens, and C. Bretherton (2015): Adjustments in the forcing feedback framework for understanding climate change, *Bull. Am. Meteorol. Soc.*, 96, 217–228, doi:10.1175/BAMS-D-13-00167.1.

Shindell, D. T., G. Faluvegi, N. Bell, and G. A. Schmidt (2005): An emissions-based view of climate forcing by methane and tropospheric ozone, *Geophys. Res. Lett.*, 32, L04803, doi:10.1029/2004GL021900.

Shindell, D. T., Faluvegi, G., Koch, D. M., Schmidt, G. A., Unger, N., and Bauer, S. E. (2009): Improved attribution of climate forcing to emissions, *Science*, 326, 716–718, doi:10.1126/science.1174760.

Shindell, D., G. Faluvegi, L. Nazarenko, K. Bowman, J.-F. Lamarque, A. Voulgarakis, G. A. Schmidt, O. Pechony and R. Ruedy (2013a): Attribution of historical ozone forcing to anthropogenic emissions, *Nature Climate Change*, 3, pp. 567–570.

Shindell, D. T., Pechony, O., Voulgarakis, A.., Faluvegi, G., Milly, G., Kovari, B., Ruedy, R., and G. A. Schmidt (2013b): Interactive ozone and methane chemistry in GISS-E2 historical and future climate simulations, *Atmos. Chem. Phys.*, 13, 2653–2689, doi:10.5194/acp-13-2653-2013.

Shine K. P., B. P. Briegleb, A. S. Grossman, D. Hauglustaine, Huiting Mao, V. Ramaswamy, M. D. Schwarzkopf, R. Van Dorland, W.-C. Wang (1995): Radiative forcing due to changes in ozone: a comparison of different codes. In: Wang W.-C., Isaksen I.S.A. (eds) Atmospheric Ozone as a Climate Gas. NATO ASI Series (Series I: Global Environmental Change), vol 32. Springer, Berlin, Heidelberg.

Shine, K. P., and P. M. de F. Forster (1999): The effect of human activity on radiative forcing of climate change: a review of recent developments, *Global Planet. Change*, 20, 1999, 205–225.

Sitch, S., Cox, P. M., Collins, W. J., and Huntingford, C. (2007): Indirect radiative forcing of climate change through ozone effects on the land-carbon sink, *Nature*, 448, 791–794, doi:10.1038/nature06059.

Skeie, R. B., T. K. Berntsen, G. Myhre, K. Tanaka, M. M. Kvalevåg, and C. R. Hoyle (2011): Anthropogenic radiative forcing time series from pre-industrial times until 2010, *Atmos. Chem. Phys.*, 11, 11827–11857, doi:10.5194/acp-11-11827-2011.

Smith, C. J., R. J. Kramer, G. Myhre, G., P. M. Forster, B. J. Soden, T. Andrews, O. Boucher, G. Faluvegi, D. Fläschner, Ø. Hodnebrog, M. Kasoar, V. Kharin, A. Kirkevåg, J.-F. Lamarque, J. Mülmenstädt, D. Olivié, T. Richardson, B. H. Samset, D. Shindell, P. Stier, T. Takemura, A. Voulgarakis, and D. Watson-Parris (2018): Understanding rapid adjustments to diverse forcing agents, *Geophys. Res. Lett.*, 45, 12023–12031, doi.org/10.1029/2018GL079826.

Soden, B.J., I.M. Held, R. Colman, K.M. Shell, J.T. Kiehl, and C.A. Shields (2008): Quantifying Climate Feedbacks Using Radiative Kernels. *J. Climate,* 21, 3504–3520, doi.org/10.1175/2007JCLI2110.1.

Stevenson, D. S., P. J. Young, V. Naik, J.-F. Lamarque, D. T. Shindell, A. Voulgarakis, R. B. Skeie, S. B. Dalsoren, G. Myhre, T. K. Berntsen, G. A. Folberth, S. T. Rumbold, W. J. Collins, I. A. MacKenzie, R. M. Doherty, G. Zeng, T. P. C. van Noije, A. Strunk, D. Bergmann, P. Cameron-Smith, D. A. Plummer 13 , S. A. Strode, L. Horowitz , Y. H. Lee , S. Szopa , K. Sudo , T. Nagashima , B. Josse, I. Cionni, M. Righi, V. Eyring , A. Conley , K. W. Bowman , O. Wild, and A. Archibald (2013):

Tropospheric ozone changes, radiative forcing and attribution to emissions in the Atmospheric Chemistry and Climate Model Intercomparison Project (ACCMIP), *Atmos. Chem. Phys.*, 13, 3063–3085, doi:10.5194/acp-13-3063-2013.

1370

Stjern, C. W., Samset, B. H., Myhre, G., Forster, P. M., Hodnebrog, Ø. Andrews, T., O. Boucher, G. Faluvegi, T. Iversen, M. Kasoar, V. Kharin, A. Kirkevåg, J.-F. Lamarque, D. Olivié, T. Richardson, D. Shawki, D. Shindell, C. J. Smith, T. Takemura, and A. Voulgarakis (2017): Rapid adjustments cause weak surface temperature response to increased black carbon concentrations, *J. Geophys. Res.: Atmos.*, 122, 11462– 11481, doi.org/10.1002/2017JD027326.

1375

Søvde, O., C. Hoyle, G. Myhre, and I. Isaksen (2011): The HNO3 forming branch of the HO2 + NO reaction: Pre-industrial-to-present trends in atmospheric species and radiative forcings, *Atmos. Chem. Phys.*, 11, 8929–8943.

Taylor, K. E., Stouffer, R. J., and Meehl, G. A. (2012): An Overview of CMIP5 and the Experiment Design, *B. Am. Meteorol.*
1380   *Soc.*, 93, 485–498.

Teixeira, J. C., et al. (2019): Resampling Hypothesis for Testing Reproducibility of Earth System models, In preparation.

Thomason, L. W., N. Ernest, L. Millán, L. Rieger, A. Bourassa, J.-P. Vernier, G. Manney, B. Luo, F. Arfeuille, and T. Peter
1385   (2018): A global space-based stratospheric aerosol climatology: 1979–2016, *Earth Syst. Sci. Data*, 10, 469–492, doi.org/10.5194/essd-10-469-2018.

Thornhill, G., et al. (2019): Effective Radiative forcing from emissions of reactive gases and aerosols, In preparation.

1390   Toll, V., Christensen, M., Gassó, S., and Bellouin, N. (2017): Volcano and ship tracks indicate excessive aerosol-induced cloud water increases in a climate model, *Geophys. Res. Lett.*, 44, 12492–12500, doi.org/10.1002/2017GL075280.

Turnock, S., O. Wild, F. Dentener, Y. Davila, L. Emmons, J. Flemming, G. Folberth, D. Henze, J. Jonson, T. Keating, S. Kengo, M. Lin, M. Lund, S. Tilmes, and F. M. O'Connor (2018):The Impact of Future Emission Policies on Tropospheric
1395   Ozone using a Parameterised Approach, *Atmos. Chem. Phys.*, 18, 8953–8978, doi.org/10.5194/acp-18-8953-2018.

Turnock, S. T., Wild, O., Sellar, A., and O'Connor, F. M. (2019), 300 years of tropospheric ozone changes using CMIP6 scenarios with a parameterised approach, *Atmos. Environ.,* 213, 686-698, doi.org/10.1016/j.atmosenv.2019.07.001.

1400   Twomey, S. (1977): The Influence of Pollution on the Shortwave Albedo of Clouds. *J. Atmos. Sci.,* 34, 1149–1152, https://doi.org/10.1175/1520-0469(1977)034<1149:TIOPOT>2.0.CO;2.

Voulgarakis, A., Naik, V., Lamarque, J.-F., Shindell, D. T., Young, P. J., Prather, M. J., Wild, O., Field, R. D., Bergmann, D., Cameron-Smith, P., Cionni, I., Collins, W. J., Dalsøren, S. B., Doherty, R. M., Eyring, V., Faluvegi, G., Folberth, G. A.,
1405   Horowitz, L. W., Josse, B., MacKenzie, I. A., Nagashima, T., Plummer, D. A., Righi, M., Rumbold, S. T., Stevenson, D. S., Strode, S. A., Sudo, K., Szopa, S., and Zeng, G. (2013): Analysis of present day and future OH and methane lifetime in the ACCMIP simulations, *Atmos. Chem. Phys.*, 13, 2563–2587, doi.org/10.5194/acp-13-2563-2013.

Walters, D., A. J. Baran, I. Boutle, M. Brooks, P. Earnshaw, J. Edwards, K. Furtado, P. Hill, A. Lock, J. Manners, C. Morcrette,
1410   J. Mulcahy, C. Sanchez, C. Smith, R. Stratton, W. Tennant, L. Tomassini, K. Van Weverberg, S. Vosper, M. Willett, J. Browse, A. Bushell, K. Carslaw, M. Dalvi, R. Essery, N. Gedney, S. Hardiman, B. Johnson, C. Johnson, A. Jones, C. Jones, G. Mann, S. Milton, H. Rumbold, A. Sellar, M. Ujiie, M. Whitall, K. Williams, and M. Zerroukat (2019), The Met Office Unified Model Global Atmosphere 7.0/7.1 and JULES Global Land 7.0 configurations, *Geosci. Model Dev.*, 12, 1909–1963, doi.org/10.5194/gmd-12-1909-2019.

1415

Wild, O., A. Voulgarakis, F. O'Connor, J.-F. Lamarque, E. M. Ryan, and L. Lee (2019): Global sensitivity analysis of chemistry-climate model budgets of tropospheric ozone and OH: Exploring model diversity, *Atmos. Chem. Phys. Disc.*, doi.org/10.5194/acp-2019-774.

1420 Wilks, D.S. (1997): Resampling hypothesis tests for autocorrelated fields, *J. Climate*, 10(1), 65-82.

Williams, K. D., Copsey, D., Blockley, E. W., Bodas-Salcedo, A., Calvert, D., Comer, R., P. Davis, T. Graham, H. T. Hewitt, R. Hill, P. Hyder, S. Ineson, T. C. Johns, A. B. Keen, R. W. Lee, A. Megann, S. F. Milton, J. G. L. Rae, M. J. Roberts, A. A. Scaife, R. Schiemann, D. Storkey, L. Thorpe, I. G. Watterson, D. N. Walters, A. West, R. A. Wood, T. Woollings, and Xavier,
1425 P. K. (2017): The Met Office Global Coupled model 3.0 and 3.1 (GC3.0 and GC3.1) configurations, *J. Adv. Modeling Earth Systems*, 10, 357–380, doi.org/10.1002/2017MS001115.

Winterstein, F., F. Tanalski, P. Jöckel, M. Dameris, and M. Ponater (2019): Implication of strongly increased atmospheric methane concentrations for chemistry–climate connections, *Atmos. Chem. Phys.*, 19, 7151–7163, doi:10.5194/acp-19-
1430 7151-2019.

Xia, Y., Hu, Y., and Huang, Y. (2016): Strong modification of stratospheric ozone forcing by cloud and sea-ice adjustments, *Atmos. Chem. Phys.,* 16, 7559–7567.

1435 Xing, J., J. Wang, R. Mathur, S. Wang, G. Sarwar, J. Pleim, C. Hogrefe, Y. Zhang, J. Jiang, D. Wong, and J. Hao (2017): Impacts of aerosol direct effects on tropospheric ozone through changes in atmospheric dynamics and photolysis rates, *Atmos. Chem. Phys.*, 17, 9869-9883, doi:10.5194/acp-17-9869-2017.

Yeung, L.Y., Murray, L.T., P. Martinerie, E. Witrant, H. Hu, A. Banerjee, A. Orsi, and J. Chappellaz (2019): Isotopic
1440 constraint on the twentieth-century increase in tropospheric ozone. *Nature,* 570, 224–227, doi:10.1038/s41586-019-1277-1.

Young, P. J., A. T. Archibald, K. W. Bowman, J.-F. Lamarque, V. Naik, D. S. Stevenson, S. Tilmes, A. Voulgarakis, O. Wild, D. Bergmann, P. Cameron-Smith, I. Cionni, W. J. Collins, S. B. Dalsøren, R. M. Doherty, V. Eyring, G. Faluvegi, L. W. Horowitz, B. Josse, Y. H. Lee, I. A. MacKenzie8 , T. Nagashima, D. A. Plummer, M. Righi, S. T. Rumbold, R. B. Skeie, D.
1445 T. Shindell, S. A. Strode, K. Sudo, S. Szopa, and G. Zeng (2013): Pre-industrial to end 21st century projections of tropospheric ozone from the Atmospheric Chemistry and Climate Model Intercomparison Project (ACCMIP), *Atmos. Chem. Phys.*, 13, 2063-2090, doi:10.5194/acp-13-2063-2013.

Young, P. J., Naik, V., Fiore, A. M., Gaudel, A., Guo, J., Lin, M. Y., Neu, J. L., Parrish, D. D., Rieder, H. E., Schnell, J. L.,
1450 Tilmes, S., Wild, O., Zhang, L., Ziemke, J. R., Brandt, J., Delcloo, A., Doherty, R. M., Geels, C., Hegglin, M. I., Hu, L., Im, U., Kumar, R., Luhar, A., Murray, L., Plummer, D., Rodriguez, J., Saiz-Lopez, A., Schultz, M. G., Woodhouse, M. T. and Zeng, G. (2018): Tropospheric Ozone Assessment Report: Assessment of global-scale model performance for global and regional ozone distributions, variability, and trends, *Elem. Sci. Anth.*, 6(1), p.10, doi.org/10.1525/elementa.265.

1455 Zelinka, M. D., Andrews, T., Forster, P. M., and Taylor, K. E. (2014): Quantifying components of aerosol-cloud-radiation interactions in climate models, *J. Geophys. Res. Atmos.*, 119, 7599– 7615, doi:10.1002/2014JD021710.